J. Fluid Mech. (2018), *vol.* 837, *pp.* 258–292. © Cambridge University Press 2017
doi:10.1017/jfm.2017.847

Vortex-induced vibration of a rotating sphere

A. Sareen[1], J. Zhao[1,†], D. Lo Jacono[2], J. Sheridan[1], K. Hourigan[1] and M. C. Thompson[1]

[1]Fluids Laboratory for Aeronautical and Industrial Research (FLAIR), Department of Mechanical and Aerospace Engineering, Monash University, Melbourne, VIC 3800, Australia

[2]Institut de Mécanique des Fluides de Toulouse (IMFT), Université de Toulouse, CNRS, Toulouse, France

(Received 6 March 2017; revised 13 October 2017; accepted 16 November 2017)

Vortex-induced vibration (VIV) of a sphere represents one of the most generic fundamental fluid–structure interaction problems. Since vortex-induced vibration can lead to structural failure, numerous studies have focused on understanding the underlying principles of VIV and its suppression. This paper reports on an experimental investigation of the effect of imposed axial rotation on the dynamics of vortex-induced vibration of a sphere that is free to oscillate in the cross-flow direction, by employing simultaneous displacement and force measurements. The VIV response was investigated over a wide range of reduced velocities (i.e. velocity normalised by the natural frequency of the system): $3 \leqslant U^* \leqslant 18$, corresponding to a Reynolds number range of $5000 < Re < 30\,000$, while the rotation ratio, defined as the ratio between the sphere surface and inflow speeds, $\alpha = |\omega|D/(2U)$, was varied in increments over the range of $0 \leqslant \alpha \leqslant 7.5$. It is found that the vibration amplitude exhibits a typical inverted bell-shaped variation with reduced velocity, similar to the classic VIV response for a non-rotating sphere but without the higher reduced velocity response tail. The vibration amplitude decreases monotonically and gradually as the imposed transverse rotation rate is increased up to $\alpha = 6$, beyond which the body vibration is significantly reduced. The synchronisation regime, defined as the reduced velocity range where large vibrations close to the natural frequency are observed, also becomes narrower as α is increased, with the peak saturation amplitude observed at progressively lower reduced velocities. In addition, for small rotation rates, the peak amplitude decreases almost linearly with α. The imposed rotation not only reduces vibration amplitudes, but also makes the body vibrations less periodic. The frequency spectra revealed the occurrence of a broadband spectrum with an increase in the imposed rotation rate. Recurrence analysis of the structural vibration response demonstrated a transition from periodic to chaotic in a modified recurrence map complementing the appearance of broadband spectra at the onset of bifurcation. Despite considerable changes in flow structure, the vortex phase (ϕ_{vortex}), defined as the phase between the vortex force and the body displacement, follows the same pattern as for the non-rotating case, with the ϕ_{vortex} increasing gradually from low values in Mode I of the sphere vibration to almost 180° as the system undergoes a continuous transition to Mode II of the sphere vibration at higher reduced velocity. The total phase (ϕ_{total}), defined as the phase between the transverse lift force and the body displacement, only increases from low values after the peak amplitude

† Email address for correspondence: jisheng.zhao@monash.edu

response in Mode II has been reached. It reaches its maximum value ($\sim$165°) close to the transition from the Mode II upper plateau to the lower plateau, reminiscent of the behaviour seen for the upper to lower branch transition for cylinder VIV. Hydrogen-bubble visualisations and particle image velocimetry (PIV) performed in the equatorial plane provided further insights into the flow dynamics near the sphere surface. The mean wake is found to be deflected towards the advancing side of the sphere, associated with an increase in the Magnus force. For higher rotation ratios, the near-wake rear recirculation zone is absent and the flow is highly vectored from the retreating side to the advancing side, giving rise to large-scale shedding. For a very high rotation ratio of $\alpha = 6$, for which vibrations are found to be suppressed, a one-sided large-scale shedding pattern is observed, similar to the shear-layer instability one-sided shedding observed previously for a rigidly mounted rotating sphere.

Key words: flow–structure interactions, vortex streets, wakes

1. Introduction

Vortex-induced vibration (VIV) of structures can occur in a variety of engineering situations, such as with flows past bridges, transmission lines, aircraft control surfaces, offshore structures, engines, heat exchangers, marine cables, towed cables, drilling and production risers in petroleum production, moored structures, tethered structures, pipelines and other hydrodynamic and hydroacoustic applications. VIV is a significant cause of fatigue damage that can lead to structural failures. Numerous studies have focused on understanding the underlying principles of flow-induced vibrations and its suppression, especially for cylinders. The immense practical significance of VIV has led to various comprehensive reviews, including Bearman (1984), Blevins (1990), Sarpkaya (2004), Williamson & Govardhan (2004), Païdoussis, Price & De Langre (2010) and Naudascher & Rockwell (2012). However, unlike the situation for cylinders, there are relatively fewer studies on VIV of elastically mounted or tethered spheres (e.g. Govardhan & Williamson 1997; Williamson & Govardhan 1997; Jauvtis, Govardhan & Williamson 2001; Pregnalato 2003; Govardhan & Williamson 2005; van Hout, Krakovich & Gottlieb 2010; Behara, Borazjani & Sotiropoulos 2011; Krakovich, Eshbal & van Hout 2013; Lee, Hourigan & Thompson 2013; van Hout, Katz & Greenblatt 2013*a*,*b*; Behara & Sotiropoulos 2016), despite its ubiquitous practical significance, such as marine buoys, underwater mines, other offshore structures and tethered or towed spherical objects. Because of the geometric shape of the body, VIV of a sphere represents one of the most fundamental fluid–structure interaction problems. It is a generic symmetrical three-dimensional prototype, and improved understanding of VIV of a sphere provides a framework to comprehend VIV of more complex three-dimensional bluff bodies around us.

Govardhan & Williamson (1997) and Williamson & Govardhan (1997) reported, for the first time, the dynamics and forcing of a tethered sphere in a fluid flow. They found that a tethered sphere could oscillate at a saturation peak-to-peak amplitude of close to two body diameters. Jauvtis *et al.* (2001) discovered the existence of multiple modes of vortex-induced vibration of a tethered sphere in a free stream, namely Modes I, II and III. The first two modes, which occur over a velocity range of $U^* \sim 5$–10, were associated with lock-in of the system natural frequency with the vortex formation frequency, as occurs for the 2S and 2P modes for an excited cylinder. However, Mode III, which occurs over a broad range of high velocity

ranging from $U^* \sim 20$–40, does not have any apparent counterpart in the circular cylinder VIV case. This was later categorised and explained as a 'movement-induced vibration' by Govardhan & Williamson (2005). They further found an unsteady mode of vibration, Mode IV, at very high reduced velocities, characterised by intermittent bursts of large-amplitude vibration. The physical origin of such a mode of vibration still remains unknown.

Previous numerical studies on the effect of rotation on rigidly mounted rotating spheres at low Reynolds numbers ($Re \leqslant 300$) (Kim 2009; Poon *et al.* 2014) have revealed suppression of the vortex shedding for a certain range of rotation rates. These studies were performed computationally at relatively low Reynolds numbers. On the other hand, there have been some experimental studies conducted at considerably higher Reynolds numbers ($Re \geqslant 6 \times 10^4$) that focus mainly on the effect of transverse rotation on the fluid forces, e.g. the inverse Magnus effect (Macoll 1928; Barlow & Domanski 2008; Kray, Franke & Frank 2012; Kim *et al.* 2014), where the rotation-induced lift suddenly changes direction as the Reynolds number is increased. It is still unknown if the rotation suppresses vortex shedding at such high Reynolds numbers. Nevertheless, all these studies have observed a sudden dip in the lift and drag coefficients for a certain rotation ratio (which varies with Re). The question arises as to whether imposed rotation can suppress VIV of an elastically mounted sphere.

Bourguet & Lo Jacono (2014) studied computationally the effect of imposed transverse rotation on the VIV response of a circular cylinder at $Re = 100$. Notably, they found that the peak amplitude increases to $\sim$1.9 cylinder diameters, which is three times that of the non-rotating case, as the rotation ratio was increased from 0 to 3.75. An extensive experimental study by Wong *et al.* (2017) on the effect of imposed rotation on the VIV response of a circular cylinder for $1100 \leqslant Re \leqslant 6300$ also demonstrated an increase of up to $\sim$80 % in the peak oscillation amplitude over the non-rotating case for rotation rates less than 2. In contrast, Seyed-Aghazadeh & Modarres-Sadeghi (2015) studied the same problem experimentally, over the Reynolds number range $Re = 350$–1000. In this case, the amplitude response was found to only increase marginally with rotation rate, increasing from 0.5 to 0.6 as the rotation ratio was increased up to 2.4. Thus, even for VIV of a rotating cylinder there appear to be conflicting results on the effect of rotation on the VIV response.

One question to be addressed is whether similar features are exhibited in the case of a rotating sphere. Specifically, this paper examines the effect of the body rotation on the VIV response of an elastically mounted sphere. This study addresses the following fundamental questions: How does constant imposed transverse rotation affect the VIV response of the sphere, does it suppress or enhance the response and how does this depend on rotation rate? How does the rotation affect the flow near the sphere surface and in the wake?

The experimental method used in the current study is detailed in § 2, and a validation study based on VIV of a non-rotating oscillating sphere is given in § 3. In § 4, the results and discussion on VIV of a rotating sphere are presented. Following this, § 5 focuses on analysis of flow visualisations and finally § 6 draws conclusions for the important findings and the significance of the current study.

2. Experimental method

2.1. *Fluid–structure system*

A schematic showing the experimental arrangement for the problem of one-degree-of-freedom (1-DOF) transverse VIV of a rotating sphere is presented in figure 1. The elastically mounted sphere is free to oscillate in only one direction transverse to the

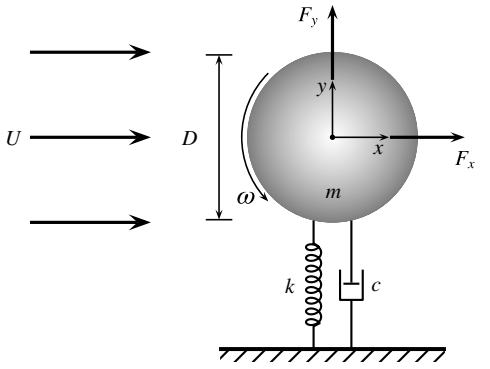

FIGURE 1. Definition sketch for the transverse vortex-induced vibration of a rotating sphere. The hydro-elastic system is simplified as a 1-DOF system constrained to move in the cross-flow direction. The axis of rotation is transverse to both the flow direction (x-axis) and the oscillation axis (y-axis). Here, U is the free-stream velocity, k the spring constant, D the sphere diameter, m the oscillating mass, c the structural damping, ω the angular velocity. F_x and F_y represent the streamwise (drag) and the transverse (lift) force components acting on the body, respectively.

Amplitude ratio	A^*	A/D
Amplitude ratio	A^*_{10}	A_{10}/D
Damping ratio	ζ	$c/2\sqrt{k(m+m_A)}$
Frequency ratio	f^*	f/f_{nw}
Mass ratio	m^*	m/m_d
Mass-damping parameter	ξ	$(m^*+C_A)\zeta$
Rotation ratio	α	$\lvert\omega\rvert D/(2U)$
Reduced velocity	U^*	$U/(f_{nw}D)$
Reynolds number	Re	UD/ν
Scaled normalised velocity	U^*_S	$(U^*/f^*)S = f_{vo}/f$
Strouhal number	S	$f_{vo}D/U$

TABLE 1. Non-dimensional parameters used in this study. In the above parameters, A is the structural vibration amplitude in the y direction, and A_{10} represents the mean of the top 10 % of amplitudes. D is sphere diameter; f is the body oscillation frequency and f_{nw} is the natural frequency of the system in quiescent water. m is the total oscillating mass, c is the structural damping factor and k is the spring constant; U is the free-stream velocity, and ν is the kinematic viscosity; m_A denotes the added mass, defined by $m_A = C_A m_d$, where m_d is the mass of the displaced fluid and C_A is the added-mass coefficient (0.5 for a sphere); $\omega =$ rotational speed of the sphere; f_{vo} is the vortex shedding frequency of a fixed body.

oncoming flow. The axis of rotation is perpendicular to both the flow direction and the oscillation axis.

Table 1 presents the set of the relevant non-dimensional parameters in the current study. In studies of flow-induced vibration (FIV) of bluff bodies, the dynamics of the system is often characterised by the normalised structural vibration amplitude (A^*) and frequency (f^*) responses as a function of reduced velocity. Note that A^* here

is defined by $A^* = \sqrt{2}A_{rms}/D$, where A_{rms} is the root mean square (r.m.s.) oscillation amplitude of the body. The reduced velocity here is defined by $U^* = U/(f_{nw}D)$, where f_{nw} is the natural frequency of the system in quiescent water. The mass ratio, an important parameter in the fluid–structure system, is defined as the ratio of the mass of the system (m) to the displaced mass of the fluid (m_d), namely $m^* = m/m_d$, where $m_d = \rho\pi D^3/6$ with ρ being the fluid density. The non-dimensional rotation ratio, as a measure of the ratio between the equatorial speed of the sphere to the free-stream speed, is defined by $\alpha = |\omega|D/(2U)$, where ω is the angular velocity of the sphere. Physically, the rotation rate quantifies how fast the surface of the sphere is spinning relative to the incoming flow velocity. The Reynolds number based on the sphere diameter is defined by $Re = UD/\nu$.

The governing equation for motion characterising cross-flow VIV of a sphere can be written as

$$m\ddot{y} + c\dot{y} + ky = F_y, \tag{2.1}$$

where F_y represents fluid force in the transverse direction, m is the total oscillating mass of the system, c is the structural damping of the system, k is the spring constant and y is the displacement in the transverse direction. Using the above equation, the fluid force acting on the sphere can be calculated with the knowledge of the directly measured displacement, and its time derivatives.

2.2. *Experimental details*

The experiments were conducted in the recirculating free-surface water channel of the Fluids Laboratory for Aeronautical and Industrial Research (FLAIR), Monash University, Australia. The test section of the water channel has dimensions of 600 mm in width, 800 mm in depth and 4000 mm in length. The free-stream velocity in the present experiments could be varied continuously over the range $0.05 \leqslant U \leqslant 0.45$ m s^{-1}. The free-stream turbulence level was less than 1 %. Further characterisation details of the water channel facility can be found in Zhao *et al.* (2014*a*,*b*).

A schematic of the experimental set-up is shown in figure 2. The hydro-elastic problem was modelled using a low-friction airbearing system that provided low structural damping and constrained the body motion to be in the transverse direction to the oncoming free stream. The structural stiffness was controlled by extension springs that were attached to both sides of a slider carriage. More details of the hydro-elastic facility used can be found in Zhao *et al.* (2014*a*,*b*). The sphere model was vertically supported by a thin stiff driving rod that was adapted to a rotor mechanism. The rotor mechanism was mounted to a 6-axis force sensor coupled with the carriage.

The sphere models used were solid spherical balls precision machined from acrylic plastic with a very smooth surface finish. The accuracy of the diameter was within ± 20 μm. Two sphere sizes of $D = 70$ and 80 mm were tested in the present experiments. The spherical models were supported using a cylindrical support rod 3 mm in diameter, manufactured from hardened nitrided stainless steel for extra stiffness and to maintain straightness. This gave a diameter ratio between the sphere and the support rod of 23.3. For experiments with rotation, the 3 mm support rod was supported by two miniature roller bearings, which were covered by a non-rotating cylindrical shroud 6.35 mm in diameter manufactured from stainless steel. This set-up provided extra rigidity to the support, which in turn minimised any wobbling associated with the sphere rotation, as well as limiting undesirable wake

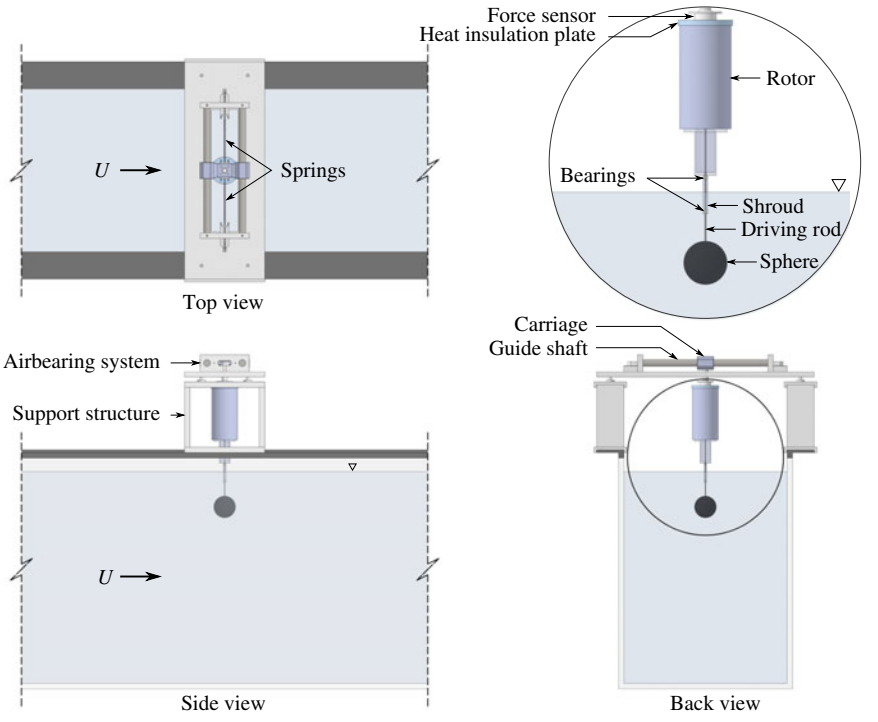

FIGURE 2. (Colour online) Schematic of the experimental set-up for the current study showing different views.

deflection that would be caused by the large Magnus force on the unshrouded rotating cylindrical rod. The immersed length of the shroud was set to approximately $0.6D$ to minimise its influence while maintaining the structural support for the driving rod having an immersed length of $0.5D$ exposed beyond the shroud. The total immersed length of the support set-up for the sphere was approximately $1.1D$. A preliminary study by Mirauda, Volpe Plantamura & Malavasi (2014) revealed that free-surface effects have an influence only when the immersion ratio (immersed length of the support rod/diameter of the sphere) is less than 0.5. Given this, an immersion ratio of ≈ 1 was chosen as a result of a trade-off between avoiding free-surface effects and maintaining rigidity of the support system. Furthermore, experiments were performed to determine the effect of the support rod on the amplitude response of the sphere. It was concluded that the support rod/shroud does not have any significant influence on the VIV response of the sphere for the diameter ratio (diameter of the rod/diameter of the sphere) chosen in the current study. This set-up was able to limit the wobbling deflection associated with the sphere rotation to within $\pm 1\,\%D$ for the present experiments, thereby minimising undesirable perturbations to the structural dynamics and near-body wake by stabilising the sphere's rotary motion.

The rotary motion was driven using a miniature low-voltage micro-stepping motor (model: LV172, Parker Hannifin, USA) with a resolution of 25 000 steps per revolution, which was installed inside the rotor mechanism shown in figure 2. The rotation speed was monitored using a digital optical rotary encoder (model: E5-1000, US Digital, USA) with a resolution of 4000 counts per revolution. In order to reduce heat transfer from the motor to the force sensor, an insulation plate, made from acetal

plastic, was installed between the rotor rig and the force sensor. Additionally, a small fan was used to circulate the surrounding air to dissipate the heat generated by the stepper motor. These corrective actions were found to be necessary to minimise signal drifts in the force measurement signals due to thermal effects to acceptable levels.

In the current study, two methods were employed to obtain the transverse lift. In the first method, the lift was derived from the measured displacement using (2.1). For the other method, the lift was measured directly by the force sensor, although it was still necessary to subtract the inertial term accounting for the accelerating mass below the strain gauges (which includes the sphere, support structure, rotation rig and half the mass of the force sensor) to determine the actual force on the sphere. In the current paper, for cases where the signal-to-noise ratio is too low, the theoretical force has been reported instead of the directly measured force. Where necessary, this distinction is made clear in the discussion of results that follow.

The force sensor (model: Mini40, ATI-IA, USA) provided measurements of the 6-axis force and moment components (F_x, F_y, F_z, M_x, M_y, M_z), which in particular had a resolution of $1/200$ N for F_x and F_y. This allowed accurate measurements of fluctuating lift and drag forces acting on the sphere.

The body displacement was measured using a non-contact (magnetostrictive) linear variable differential transformer (LVDT). The accuracy of the LVDT was within $\pm 0.01\,\%$ of the 250 mm range available. It was observed that signal noise of the LVDT and the force sensor could be prone to the electromagnetic noise emitted by the driving motor thereby decreasing the accuracy of the force measurements. Hence, a linear encoder (model: RGH24, Renishaw, UK) with a resolution of 1 μm was also employed to measure the displacement signal. Since the linear encoder was digital, electromagnetic noise did not affect the accuracy of the displacement signal measurement. This considerably improved accuracy and enabled reliable velocity and acceleration signals to be derived, which, in turn, enabled an accurate determination of the lift force signal as discussed above. This was tested through a direct comparison against the lift force determined by the force sensor over a wide range of U^*. It was found that the lift force measured using the force sensor matched well that derived from the linear encoder and the LVDT signals, indicating accurate measurements of the displacement and the lift force from several techniques.

The data acquisition and the controls of the flow velocity and the sphere rotation rate were automated via customised LabVIEW programs. For each data set, the signals of the displacement and force sensors were simultaneously acquired at a sampling frequency of 100 Hz for at least 100 vibration cycles.

The natural frequencies and structural damping of the system in both air and water were measured by conducting free decay tests individually in air and in quiescent water. Experiments for two mass ratios $m^* = 7.8$ and 14.2 are reported in this paper, although only the latter was used for the rotational VIV studies because of the presence of the added motor assembly in that case. The structural damping ratio with consideration of the added mass was determined to be $\zeta = 4.13 \times 10^{-3}$ and 1.46×10^{-3} for $m^* = 7.8$ and 14.2, respectively.

To gain insight into the flow dynamics, hydrogen-bubble flow visualisations were performed in the equatorial plane of the sphere. Hydrogen bubbles were generated by an upstream platinum wire of 50 μm in diameter and 500 μm in length, which was powered by a potential difference of 50 VDC. A laser sheet of ∼3 mm in thickness from a continuous laser (model: MLL-N-532-5W, CNI, China), aligned parallel to the x–y plane, was employed to illuminate the bubbles.

Vorticity field measurements were also performed in the central equatorial plane employing particle image velocimetry (PIV). For this purpose, the flow was seeded

with 13 μm hollow micro-spheres having a specific weight of 1.1 g m^{-3}. The laser arrangement was the same as described above for the hydrogen-bubble visualisations. Imaging was performed using a high-speed camera (model: Dimax S4, PCO, AG) with a resolution of 2016×2016 pixels^2. This camera was equipped with a 50 mm Nikon lens, giving a magnification of approximately 7.36 pixel mm^{-1} for the field of view. Velocity fields were deduced using in-house PIV software developed originally by Fouras, Lo Jacono & Hourigan (2008), using 32×32 pixel^2 interrogation windows in a grid layout with 50 % window overlap. All the vorticity fields shown in the current study were phase-averaged over more than 100 cycles. For each PIV measurement case, a set of 3100 image pairs were sampled at 10 Hz. Each image set was sorted into 24 phase bins based on the sphere's displacement and velocity, resulting in more than 120 image pairs for averaging at each phase. The final phase-averaged vorticity fields were smoothed slightly using an iterative Laplace filter to remove short length scale structures and to better highlight the larger-scale structures that dominate the wake.

Flow visualisations using fluorescein dye were also captured for the non-oscillating rotating sphere to better understand the effect of rotation on the near wake. For this case, the dye was injected using a thin pitot tube (1 mm in diameter) placed upstream of the sphere. Imaging was recorded using a digital camera (model: D7000, Nikon, Japan) equipped with a 50 mm lens that was positioned beneath the water channel glass floor.

In the present study, the VIV response is studied over a wide parameter space encompassing $3 \leqslant U^* \leqslant 18$ and $0 \leqslant \alpha \leqslant 7.5$. The Reynolds number for the current study varies between 5000 and 30 000.

3. VIV response of a non-rotating sphere

3.1. *Vibration response measurements*

The experimental methodologies used here were initially validated by comparing with previously published results of Govardhan & Williamson (2005) for transverse VIV of a non-rotating elastically mounted sphere. A sphere model of diameter 70 mm was used in this validation study. As described above, the sphere was supported from the top using a cylindrical support rod 3 mm in diameter with an immersed length of 90 mm. This gives a sphere to cylindrical support rod diameter of ~23 : 1. The mass ratio was $m^* = 7.8$, comparable to $m^* = 7.0$ used in experiments by Govardhan & Williamson (2005). Free decay tests were conducted individually in air and water to determine the natural frequency in air, $f_{na} = 0.495$ Hz, and in water, $f_{nw} = 0.478$ Hz. Note that these values give an added-mass coefficient of $C_A = ((f_{na}/f_{nw})^2 - 1)m^* = 0.52$, in good agreement with the known potential added mass for a sphere. The structural damping ratio was measured as $\zeta = 4.14 \times 10^{-3}$, which again was comparable to the case study with $\zeta = 4 \times 10^{-3}$ of Govardhan & Williamson (2005). For this initial study, the dynamic response of VIV was investigated over a reduced velocity range of $2.7 \leqslant U^* \leqslant 11$, corresponding to a Reynolds number range of $7000 \leqslant Re \leqslant 28\,000$. In figure 3, the amplitude response of the present study is compared directly to the response curve of Govardhan & Williamson (2005) for the similar mass ratio. The amplitude response for the higher mass ratio of $m^* = 14.2$ used for the rotating sphere experiments is also shown for comparison, as well as a significantly higher mass ratio result for $m^* = 53.7$ from Govardhan & Williamson (2005). Specifically, the non-dimensional amplitude of oscillations, A^*, is plotted as a function of the scaled reduced velocity, $U_S^* = (U^*/f^*)S \equiv f_{vo}/f$, where S is the Strouhal number for

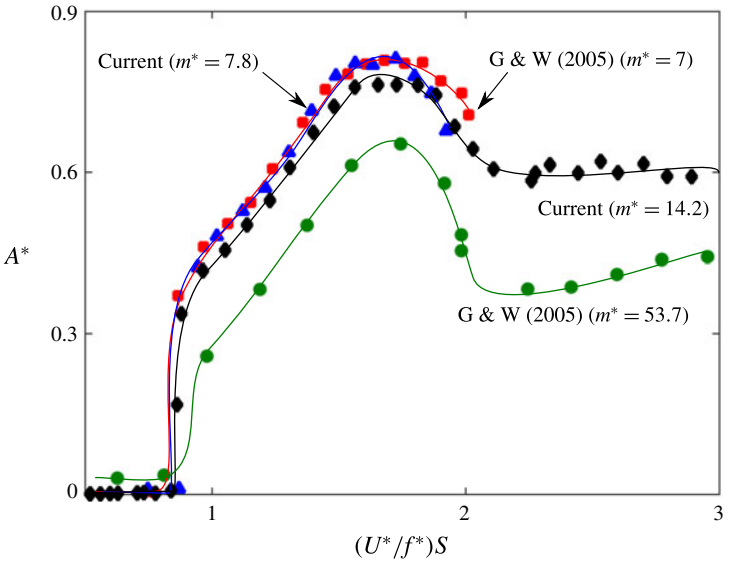

FIGURE 3. (Colour online) Comparison of the amplitude response obtained in the current study for $m^* = 7.8$ (blue triangles) to that obtained by Govardhan & Williamson (2005) for a similar mass ratio of $m^* = 7$ (red square). The response for $m^* = 14.2$ (black diamonds) from the current study is also shown along with the data by Govardhan & Williamson (2005) for significantly higher mass ratio of $m^* = 53.7$ (green circles).

the vortex shedding. Lock-in starts at $U^* = 4$–5 for the sphere, which corresponds to U_S^* of 0.7–0.875. Here, the amplitude response is plotted against U_S^* instead of U^* for the sake of direct comparison with the previous study, noting that it lines up response curves for different mass ratios. Indeed, it can be noted that using U_S^* does line up the peaks well.

It can be noted that the vibration response progresses continuously from Mode I to Mode II; indeed, the amplitude changes smoothly and continuously over the entire U^* range. This is different from the VIV response for circular cylinders, where sudden jumps are observed between the three different vibration branches. With an increase in m^* from 7.0 to 53.7, the peak amplitude in their study decreased. Similar behaviour was observed in the current study, when the mass ratio was increased, although less drastically, from 7.8 to 14.2.

For tethered spheres at higher U^*, Jauvtis *et al.* (2001) reported another vibration mode, namely Mode III. In that case, the amplitude drops to almost zero between Modes II and III, with Mode III occurring for $U_S^* \gtrsim 3$ and extending up to $\sim$8. For a 1-DOF elastically mounted sphere, the situation appears slightly different with no desynchronisation region between these modes. Instead, from the peak response in Mode II, the amplitude drops smoothly to a lower plateau that extends smoothly into Mode III as $U_S^* \to 3$. Thus, the lower plateau response branch for $U_S^* \gtrsim 2$ in figure 3 might be considered to extend towards the Mode III response at the high U^* end (Govardhan & Williamson 2005). However, recall that Mode III is characterised by a vibration response at close to the natural system frequency but far from the much higher vortex shedding frequency. For the case considered here, with $m^* = 14.2$, the vibration frequency remains close to the natural frequency over the entire range of the lower response branch as f_{vo}/f increases beyond 2. The forcing caused by vortex

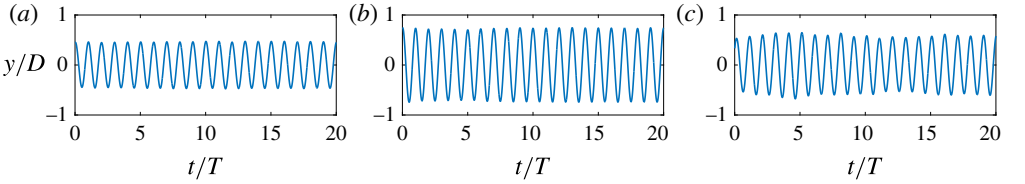

FIGURE 4. (Colour online) Strongly periodic vibrations observed for (*a*) $U^* = 6.0$ (Mode I) and (*b*) $U^* = 9.0$ (Mode II), and (*c*) slightly less periodic oscillations at the higher $U^* = 16.0$ ($\rightarrow$ Mode III).

shedding also remains at close to the natural frequency. This vibration response is very similar to the bifurcation region III reported by van Hout *et al.* (2010) for a heavy tethered sphere. They also observed less periodic, intermittent large oscillation amplitudes in the transverse direction for higher U^* values of $U^* \geqslant 15$. A Mode III response may occur beyond the U^* limit of these experiments, which was imposed by the strengths of the springs used.

Generally (near-)periodic vibrations are observed for the two fundamental vibration modes, as shown in figure 4. However, the vibrations are less periodic in the higher U^* range. More light will be shed on this in the following sections.

The comparison in figure 3 shows that the overall agreement with previous benchmark studies is excellent in terms of the two-mode amplitude response pattern, the amplitude peak value and the extent of the lock-in region.

3.2. *Force measurements for a non-rotating sphere*

As an approximation, it is often assumed that $F_y(t)$ and the response displacement $y(t)$ are both sinusoidal and represented by

$$y(t) = A \sin(2\pi f t), \tag{3.1}$$

$$F_y(t) = F_o \sin(2\pi f + \phi), \tag{3.2}$$

where F_o is the amplitude of F_y, and ϕ is the phase between the fluid force and the body displacement.

Based on the suggestions of Lighthill (1986) and as performed for VIV of a tethered sphere by Govardhan & Williamson (2000), the total transverse fluid force (F_y) can be split into a potential force ($F_{potential}$), comprising the potential added-mass force, and a vortex force component (F_{vortex}) that is due to the vorticity dynamics. From the potential theory, the instantaneous $F_{potential}$ acting on the sphere can be expressed as

$$F_{potential}(t) = -C_A m_d \ddot{y}(t). \tag{3.3}$$

Thus, the vortex force F_{vortex} can be computed from

$$F_{vortex} = F_y - F_{potential}. \tag{3.4}$$

If all the forces are normalised by $((1/2)\rho U^2 \pi D^2/4)$, this reduces to

$$C_{vortex}(t) = C_y(t) - C_{potential}(t). \tag{3.5}$$

Here, $C_{potential}$ (the potential-flow lift coefficient) can be calculated based on the instantaneous body acceleration $\ddot{y}(t)$. Reverting back to the dimensional forces for the moment, two equivalent forms can be written for the equation of motion

$$m\ddot{y} + c\dot{y} + ky = F_o \sin(\omega t + \phi_{total}), \tag{3.6}$$

and for vortex force

$$(m + m_A)\ddot{y} + c\dot{y} + ky = F_{vortex} \sin(\omega t + \phi_{vortex}). \tag{3.7}$$

The vortex phase ϕ_{vortex}, first introduced by Govardhan & Williamson (2000), is the phase difference between $C_{vortex}(t)$ and the body displacement $y(t)$. The more conventionally used total phase ϕ_{total} is the phase difference between the total force C_y and the body displacement $y(t)$. In general, phase jumps are associated with a switch from one VIV mode to another, and have even been used to distinguish between different modes (Govardhan & Williamson 2005). The instantaneous relative phases between the two forces reported in this paper are calculated using the Hilbert transform as detailed in Khalak & Williamson (1999).

According to Govardhan & Williamson (2005), there is a vortex phase shift of approximately 100° when the vibration response switches from Mode I to Mode II. They observed that the vortex phase gradually increases from ∼50 in Mode I to ∼150° as the amplitude reaches the peak response in Mode II. The change in the total phase is relatively more abrupt, and it changes from ∼0° to ∼150°; however, there is little change over the transition range between Modes I and II.

As is evident from figure 5, for the current set of experiments ($m^* = 14.2$ and $\zeta = 1.40 \times 10^{-3}$), the vortex phase and the total phase change as the vibration response switches from Mode I to Mode II, broadly following the trend of phase variations reported by Govardhan & Williamson (2005). The vortex phase starts to rise from ∼50° at the start of Mode I and reaches almost 180° towards the peak amplitude of Mode II, while the total phase only begins to rise from ∼0° as the response reaches close to the peak values in Mode II. Indeed, the total phase only reaches its maximum value of ≃160° as the Mode II response transitions from its upper to lower 'plateau'. In a sense, this appears similar to the observed behaviour for VIV of a circular cylinder. Although there are no sudden jumps or hysteresis between the branches for 1-DOF VIV of a sphere, the vortex phase and total phase transitions are broadly correlated with the initial→upper branch cylinder transition and the upper→lower branch cylinder transition, respectively, even though the phase jumps are much more gradual for the sphere transitions. Thus, the phase transitions suggest a sphere/cylinder mode equivalence for 1-DOF VIV of Mode I ≡ Initial Branch, Mode II (upper plateau) ≡ upper branch and Mode II (lower plateau) ≡ lower branch, although of course, for the sphere there is lock-in to the natural system frequency over a much wider range f_{vo}/f range than occurs for the circular cylinder. The phase jumps seem slightly more distinct in the current set of experiments than in those of Govardhan & Williamson (2005), possibly because of the lower mass ratio of $m^* = 14.2$ used here (rather than $m^* = 31.2$). Note that for a tethered sphere, for which the mode classification was developed, the response drops abruptly after the Mode II peak and hence there is no lower plateau.

Figure 6(*a*) shows the r.m.s. transverse lift coefficient as a function of U^* for $m^* = 14.2$. It can be noted that $C'_{y_{rms}}$ jumps up at the beginning of Mode I at the onset of lock-in, and steadily decreases as the response transitions to Mode II. It remains almost constant beyond $U^* = 10$. Figure 6(*b*) shows the variation of the

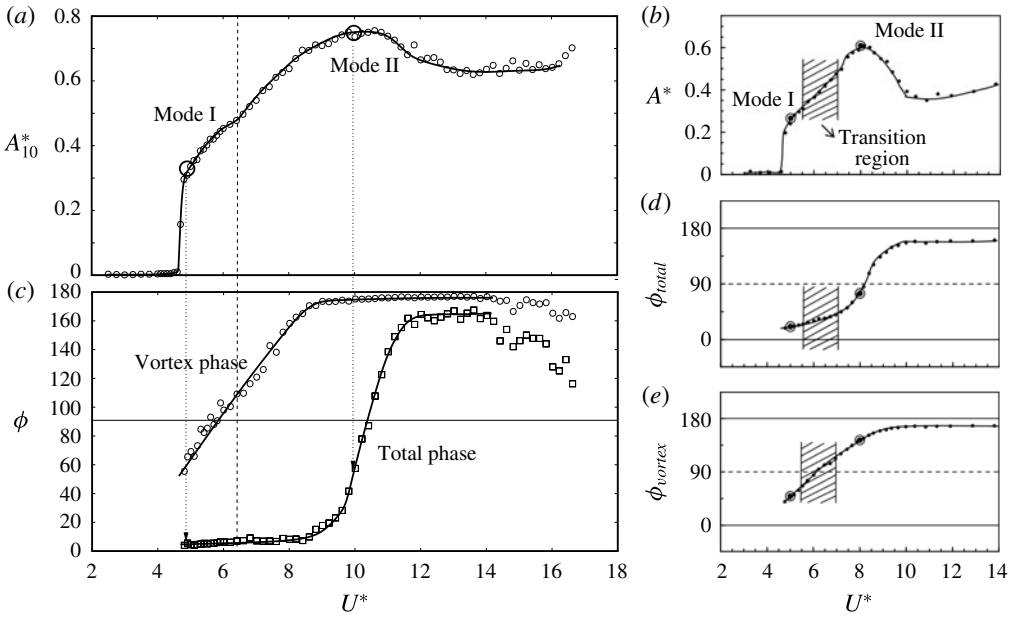

FIGURE 5. Variation of the total phase (ϕ_{total}) and the vortex phase (ϕ_{vortex}) with U^*. (*a,c*) measured phase variations (*c*) correlated with the amplitude response curve (*a*). The vortex phase starts to rise from ∼50° at the start of Mode I, while the total phase only begins to rise from ∼0° as the response reaches close to the peak values in Mode II. The dashed line shows the approximate boundary between Modes I and II. Here, A^*_{10} is the mean of the top 10 % of amplitude peaks (as used by Hover, Miller & Triantafyllou 1997 and Morse, Govardhan & Williamson 2008). (*b,d,e*) comparison with previous results of Govardhan & Williamson (2005) (adapted with permission) for the higher mass ratio of $m^* = 31.1$.

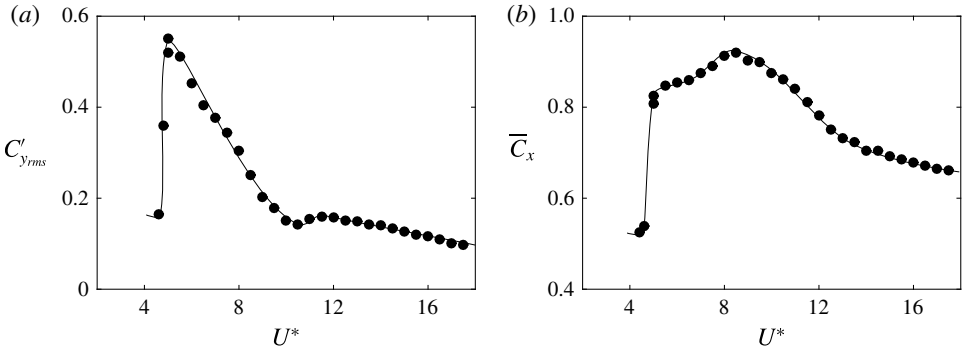

FIGURE 6. Variation of $C'_{y_{rms}}$ (*a*) and $\overline{C}_x$ (*b*) with reduced velocity.

mean drag coefficient $\overline{C}_x$ with U^*. Note that the time-mean drag coefficient does not remain constant with increasing U^*, while the sphere is oscillating. $\overline{C}_x$ also jumps up when the sphere locks in. These results are consistent with the previous observations of Govardhan & Williamson (2005) for an elastically mounted sphere but for a significantly different mass ratio and damping. A small jump in both the

coefficients is observed at $U^* \sim 10$. This is associated with the peak response in Mode II. Clear boundaries for the onset of Mode II were not known previously and ϕ_{vortex} was considered to be the criterion for distinguishing Mode II from Mode I. From this study, it is found that ϕ_{total} is also a useful criterion to distinguish between mode branches, as it jumps more abruptly, completing its transition to $\sim 165^\circ$ at the start of the lower plateau beyond the main Mode II peak. Associated jumps were observed in the force coefficients as well, again demarcating the boundaries between mode branches.

4. Effect of rotation on the VIV response of a sphere

This section focuses on VIV of an oscillating sphere subject to constant rotation. This set of experiments used a higher mass ratio of $m^* = 14.2$, because of the extra oscillating mass from the inclusion of the rotation component of the rig. The natural frequencies of the system in air and water were 0.275 Hz and 0.269 Hz, respectively, with the damping ratio of $\zeta = 1.46 \times 10^{-3}$. A sphere model of diameter 80 mm was attached to a 3 mm rod supported using a shroud support system as described previously in § 2.2. It was found that this support set-up closely reproduced the amplitude response previously reported by Govardhan & Williamson (2005). For each point in U^*–α parameter space, more than 100 oscillation periods were recorded at an acquisition rate of 100 Hz. During these experiments, for chosen values of the rotation ratio, the flow velocity was varied in small steps to obtain a wide reduced velocity range. The Reynolds number varied between 5000 and 30 000 as the reduced velocity was increased.

To investigate the effect of α on the vibration response of the sphere, U^* was varied over the range $3 \leqslant U^* \leqslant 18$, in increments of 0.5. For each U^* scan, the response was studied for discrete rotation ratios from the range $0 \leqslant \alpha \leqslant 7.5$.

4.1. *Effect of rotation on the vibration response*

The amplitude response as a function of reduced velocity is plotted in figure 7 for different rotation rates. As discussed, for $\alpha = 0$, when the sphere is not rotating, the amplitude response curve (reproduced previously in figure 3) closely matches that of Govardhan & Williamson (2005), with the amplitude of vibration gradually increasing from Mode I to Mode II, and then dropping in amplitude but still maintaining a strong oscillatory response at higher U^*. When α is increased slightly to 0.2, the amplitude response remains similar to the non-rotating case for $U^* \leqslant 8.0$; however, the A^* peak in Mode II is suppressed noticeably and the amplitude response drastically drops beyond $U^* = 14$. For $\alpha = 0.3$ and 0.4, a similar sudden drop in the response is seen at relatively lower U^* values. A sudden rebound in the amplitude response for $\alpha = 0.3$ is evident at a U^* value of $\sim$16–17. Such a rebound was also observed for $\alpha = 0.25$ and $\alpha = 0.35$. This sudden increase in the amplitude near an α value of 0.3 at higher U^* values was repeatable and was not observed for other rotation rates tested in the current study. A plausible rationale for such a rebound is discussed in § 4.3.1. For higher rotation rates ($\alpha \geqslant 0.4$), the amplitude response drops immediately after reaching the A^* peak, rather than from a plateau, as for the cases of $\alpha = 0.3$ and 0.4.

As α is increased, the U^* range over which a synchronised VIV response characterised by highly periodic large amplitude vibrations is observed becomes progressively narrower. The end of synchronisation region decreases consistently from $U^* > 20$ to $U^* \sim 7$ as α is increased from 0 to 4.0. Meanwhile, the magnitude of the

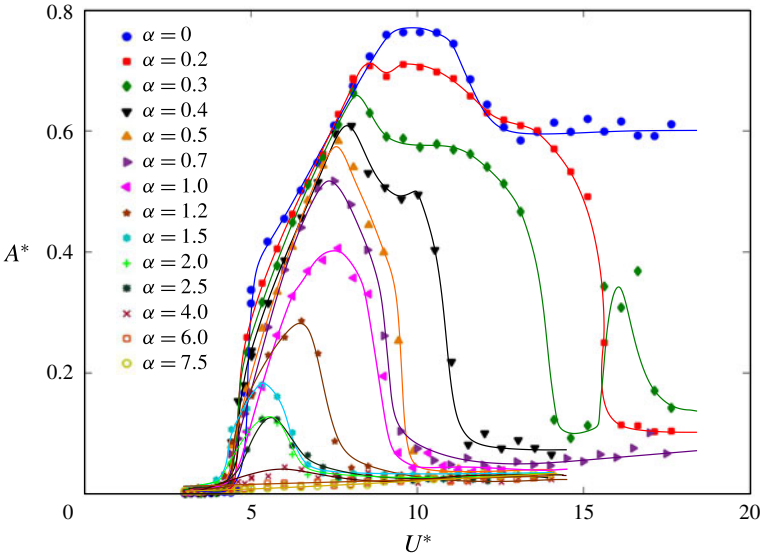

FIGURE 7. (Colour online) The vibration amplitude response as a function of reduced velocity for different rotation rates.

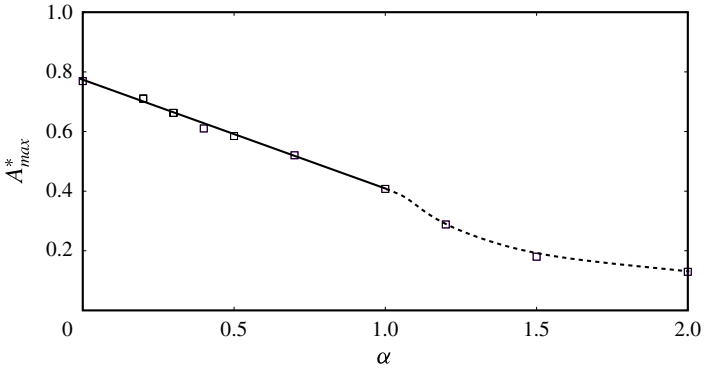

FIGURE 8. Maximum amplitude variation with rotation rate. The straight line is an approximate fit for $\alpha \leqslant 1$.

peak of amplitude response also decreases consistently from $A^* = 0.76$ to 0.03. For higher α values, no discernible peak can be detected. In addition, the peak amplitude tends to occur at a lower U^* with increasing α for $\alpha \leqslant 2$. However, for higher rotation rates, the U^* value corresponding to the A^* peak increases slightly.

Figure 8 shows the variation of the A^* peak with rotation rate. It is found that the decrease in the saturation amplitude is approximately linear with increasing rotation rate for $\alpha \lesssim 1$, and it decreases to zero more slowly beyond that α range. The overlaid straight line represents an approximate fit for the lower α range.

Figure 9 shows representative time traces of the vibration amplitude for different response branches for $\alpha = 0.5$. Similar to the case for a non-rotating sphere, the vibration is highly periodic in regions where the sphere oscillates strongly. For regions where the VIV response was found to be suppressed, the vibration was not periodic,

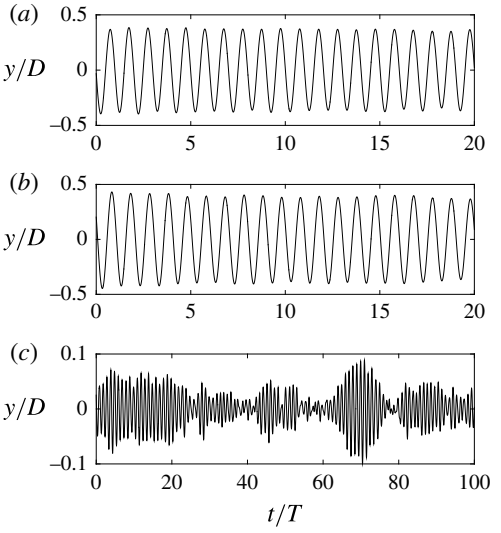

FIGURE 9. Time trace of the displacement signal at $\alpha = 0.5$ for different values of U^*. For case (*a*) $U^* = 6$, case (*b*) $U^* = 9$ and case (*c*) $U^* = 12$.

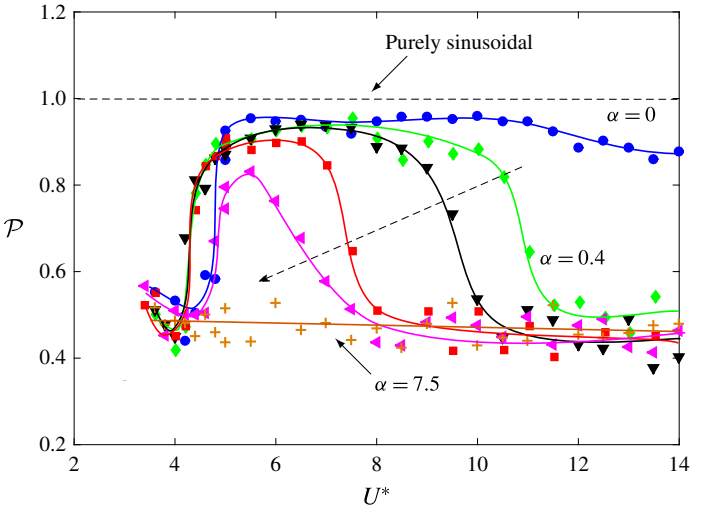

FIGURE 10. (Colour online) Variation of the periodicity, $\mathcal{P}$, versus reduced velocity for different rotation rates. The dashed line arrow indicates the direction of increasing α. Here, $\mathcal{P}$ is shown for a few representative cases of $\alpha = 0$, 0.4, 0.5, 1.2, 2.5 and 7.5.

and was characterised by intermittent bursts of vibrations, as shown in figure 9(*c*) for $U^* = 12$ and $\alpha = 0.5$. This was found to be true for all rotation rates investigated.

Following Jauvtis *et al.* (2001), the periodicity of the vibration response can be quantified by defining the periodicity, $\mathcal{P}$, of a signal as

$$\mathcal{P} = \sqrt{2} y_{rms}/y_{max}. \tag{4.1}$$

For a purely sinusoidal signal, $\mathcal{P}$ is equal to unity. Figure 10 shows how the periodicity varies with U^* for different values of α. It is evident that the response

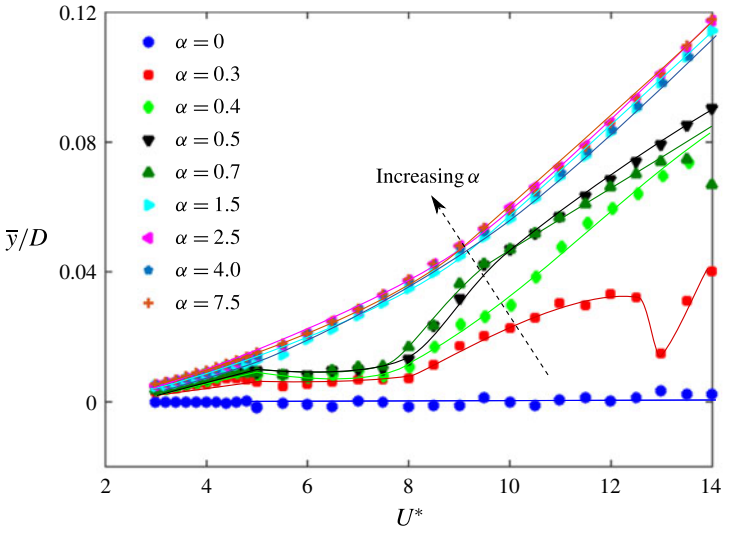

FIGURE 11. (Colour online) Variation of non-dimensional mean displacement of the sphere ($\overline{y}/D$) with the reduced velocity for different rotation rates. The dashed line arrow represents the direction of increasing α.

is highly periodic for the non-rotating case and it becomes relatively less periodic for the higher U^* values (beyond $U^* = 12$). The sphere exhibits highly periodic oscillations for $\alpha \leqslant 0.3$, but the oscillation periodicity decreases for higher α values. For higher rotation rates ($\alpha \geqslant 0.4$), it was observed that the periodicity starts to decrease as soon as the response reaches its saturation amplitude, until it reaches a plateau value, where the vibration amplitude is negligible and no further decrease in the response is observed with any further increase in U^*. Thus it can be concluded that the rotation not only decreases the amplitude of vibration but also makes the vibration less periodic.

Figure 11 shows the non-dimensional time-averaged displacement of the sphere as a function of reduced velocity for increasing rotation rates. The time-averaged displacement remains around zero for the non-rotating case, but increases with α. This is due to the rotation-induced Magnus force that exerts a one-sided fluid force acting on the sphere. It can be noted that beyond $\alpha = 1.5$, there is very slight increase in the time-averaged displacement, suggesting that the magnitude of the Magnus force is limited. Similar behaviour has also been observed in previous studies of rigidly mounted rotating spheres by Macoll (1928), Barlow & Domanski (2008), Kray *et al.* (2012) and Kim *et al.* (2014), showing that the increase in the lift coefficient of a sphere reaches a plateau as α is increased to a certain value, which depends on the Reynolds number.

Figure 12 shows logarithmic-scale power-spectrum plots depicting the dominant oscillation frequency content ($f^* = f/f_{nw}$) as a function of reduced velocity for both the non-rotating case ($\alpha = 0$) and the rotating case ($\alpha = 1$). The dashed line represents the value of f_{vo}, which is the vortex shedding frequency of a static sphere. Note that the power spectra were computed using fast Fourier transforms (FFTs) of the displacement time series for each U^* and then normalised by the maximum power. As can be seen in the figure, the dominant oscillation frequency remained close to

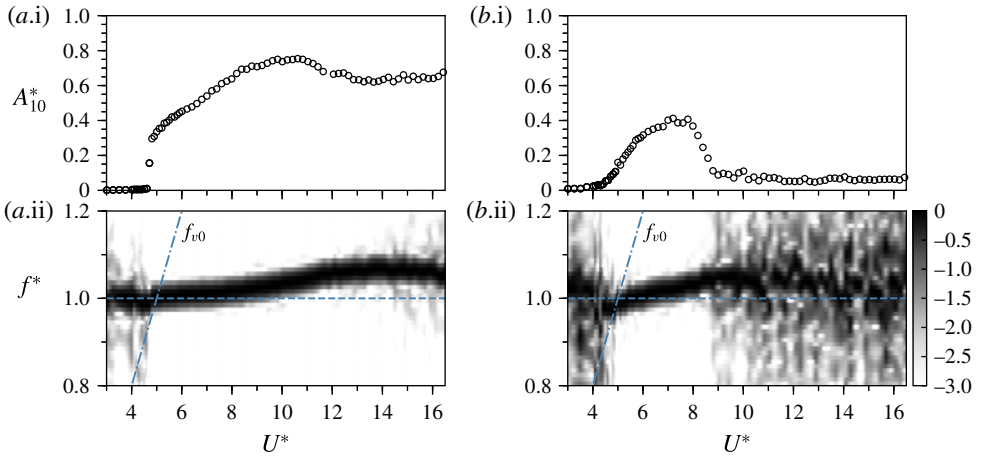

FIGURE 12. (Colour online) Frequency response as a function of U^* correlated with the amplitude response curve (above): (a.i,a.ii) $\alpha = 0$; (b.i,b.ii) $\alpha = 1$. Here, the contour map represents a logarithmic-scale power spectrum depicting the frequency ($f^* = f/f_{nw}$) content as U^* is varied. The dashed line represents the value of f_{vo}, which is the vortex shedding frequency of a static sphere.

the natural frequency of the system over the entire lock-in range for the rotating and non-rotating cases. This was found to be true for all α values investigated.

Figure 13 shows phase-space plots of the measured velocity ($\dot{y}$) (normalised by its maximum value) versus (normalised) fluctuating displacement ($\tilde{y}$) at $\alpha = 0.5$ for four different U^* values spanning the range from where the frequency response is near periodic to where it becomes chaotic. Figure 13(a) shows a relatively thin topologically circular structure corresponding to a strongly periodic sphere vibration response. On the other hand, as the sphere goes through the transition from a near periodic to less periodic response, as depicted in figure 13(b,d), the width of the phase-space region covered by successive orbits increases substantially. This is consistent with the frequency contour plots shown previously in figure 12), and the accompanying displacement time traces shown in this figure. Even at $U^* = 9.5$, where the vibration amplitude has dropped considerably from the peak response, there are signs of intermittency or mode switching, which increase at higher U^*. For an even higher U^* value of 14.0, as shown in figure 13(d), where the vibration amplitude is very small, a highly non-periodic response is observed with intermittent bursts of higher-amplitude vibrations located within an otherwise minimal response.

To add further insight to this transition, a variant of the Poincaré surface of section approach was used to further investigate the transition to non-stationary dynamics. These maps are obtained by plotting normalised sphere displacement, y/D, against its value one complete cycle previously. The points are mapped at every upward zero crossing of the sphere transverse velocity for more than 100 vibration cycles. This approach was used to explore the transition to chaos in the wake of a rolling sphere by Rao *et al.* (2012) based on numerical simulations, showing the breakdown of periodic orbits through the appearance of Kolmogorov–Arnold–Moser (KAM) tori eventually resulting in a chaotic state as the Reynolds number was further increased. Figure 14 shows such recurrence maps at $\alpha = 0.5$ for four different U^* values. As is evident from figure 14(a), at $U^* = 6$, when the vibrations are highly periodic,

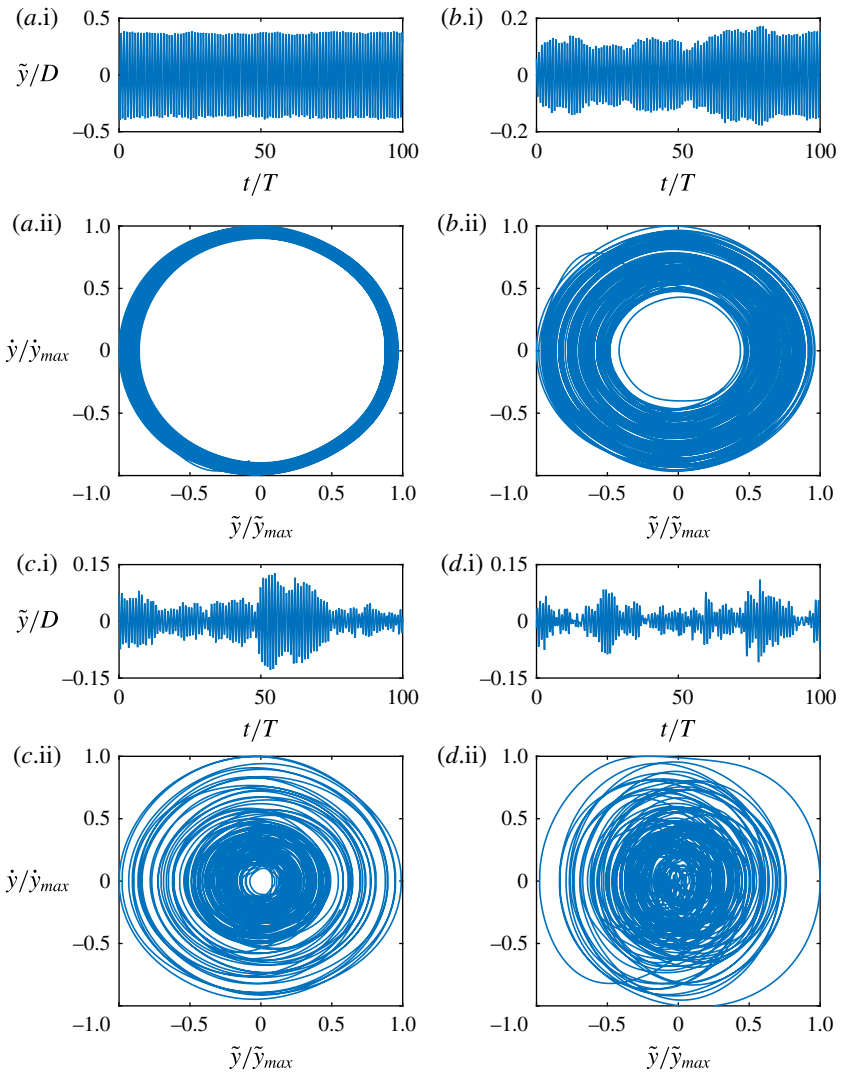

FIGURE 13. (Colour online) Phase-space plots for $\alpha = 0.5$, correlated with the time trace of the fluctuating displacement signal (above each map) at four different reduced velocities: (*a*) $U^* = 6$; (*b*) $U^* = 9.5$; (*c*) $U^* = 10.5$; (*d*) $U^* = 14.0$.

the points are clustered over a confined region of parameter space consistent with a near-periodic system state. As the U^* value is increased to higher values of $U^* = 9.5$ and $U^* = 10.5$, as shown in 14(*b*) and (*c*), respectively, the points start to spread in space, mainly along a diagonal line. For $U^* = 14.0$, the points now appear much more randomly distributed over a larger region. Together with the phase portraits and frequency spectra, this sequence of plots indicates that the system is undergoing a transition to chaotic oscillations.

To further explore how the vibration response evolves gradually from periodic to chaotic, figure 15 presents corresponding recurrence plots (RPs) based on the body displacement signal for the aforementioned four U^* values at $\alpha = 0.5$. Recurrence plots, first designed by Eckmann, Kamphorst & Ruelle (1987) to visually analyse

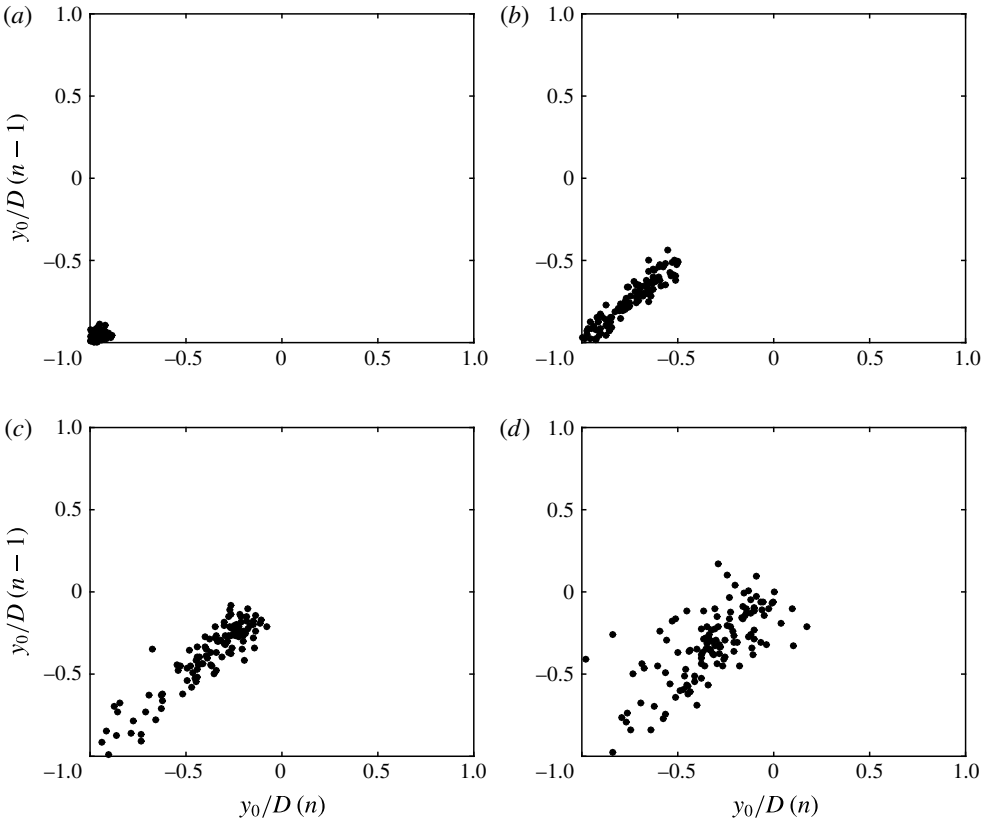

FIGURE 14. Recurrence maps for y_o/D, taken for each upward zero crossing of the sphere transverse velocity at $\alpha = 0.5$ for various U^* values: $U^* = 6$ (*a*); 9.5 (*b*); 10.5 (*c*); 14 (*d*).

the recurring patterns in time series of dynamical systems, have been utilised in a great variety of scientific areas, from physics (e.g. detection of chaos in nonlinear dynamical systems), to finance and economics, Earth science, biological systems (e.g. in cardiology, neuro-psychology), etc. A historical review of RPs has been given by Marwan (2008). The construction method for the present RPs is detailed in Marwan *et al.* (2007). As illustrated in figure 15(*a*), for the case of $U^* = 6.0$, where the body vibration is highly periodic, the RP exhibits diagonal oriented periodic checkerboard structures. These structures are symmetric about the main (45°) diagonal (also known as the line of identity (LOI)). As demonstrated in Marwan (2003) and Marwan *et al.* (2007), the diagonal lines parallel to the LOI indicate that the evolution of states of a dynamical system is similar at different epochs, while the diagonal lines orthogonal to the LOI also indicate the evolution of states of a dynamical system is similar at different epochs but with respect to reverse time. It is apparent that these diagonal lines parallel to the LOI are separated by a fixed horizontal distance matching the oscillation period, which is indicative of highly periodic recurrent dynamics with a single dominant frequency. As noted in Marwan *et al.* (2007), for a quasi-periodic system (as opposed to the current case), the distances between the diagonal lines may vary to form more complex recurrent structures. As the reduced velocity is increased to $U^* = 9.5$ and 10.5 in figures 15(*b*) and 15(*c*), respectively, the periodicity of body vibration tends to reduce with less parameter space covered by

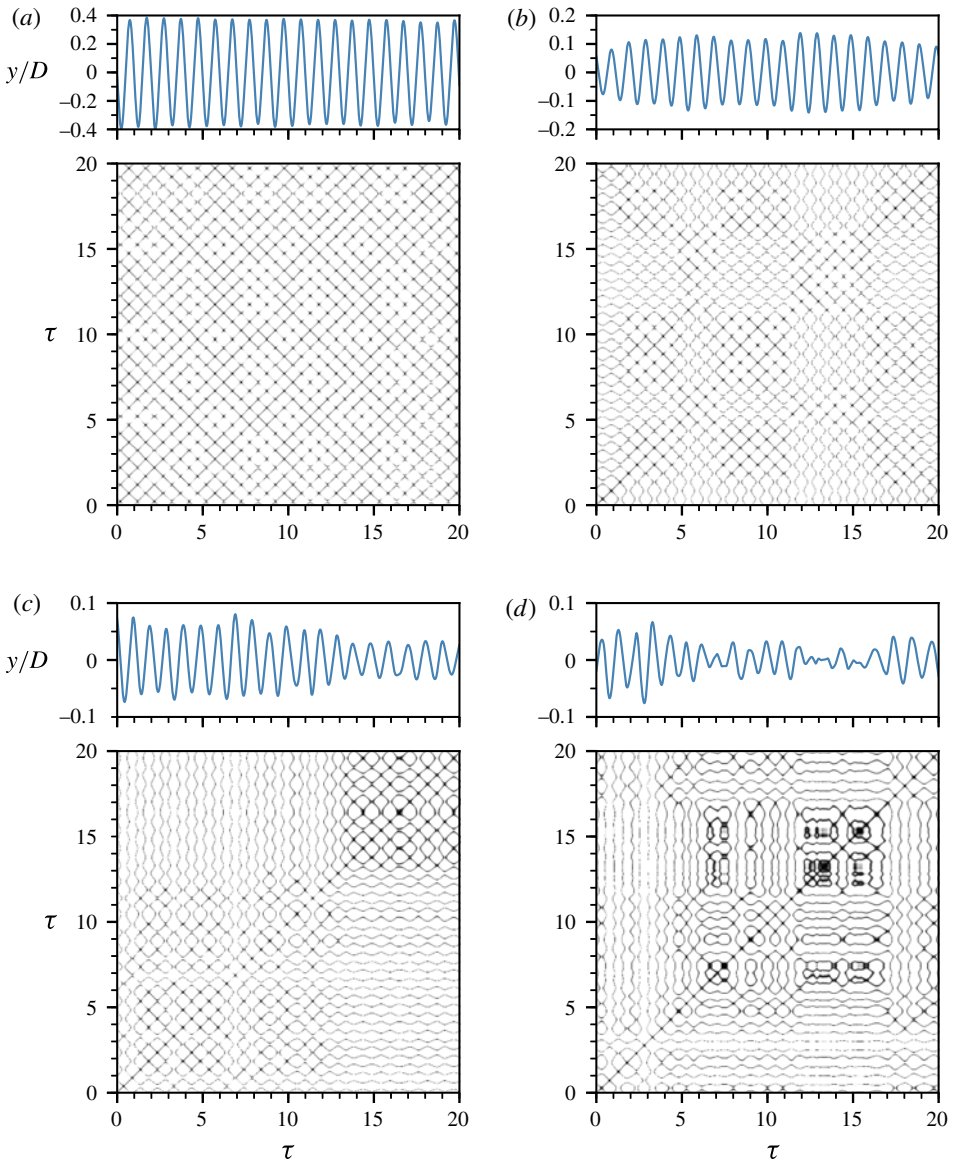

FIGURE 15. (Colour online) Recurrence plots (lower) of the time series of the normalised body displacement (upper) for $U^* = 6.0$ (*a*), 9.5 (*b*), 10.5 (*c*) and 14.0 (*d*) at $\alpha = 0.5$. Note that $\tau = t/T$ is the normalised time.

checkerboard patterns in the RPs. It should also be noted that there is an increasing trend of horizontal (and mirror vertical) curvy lines, which indicate the evolution of states of the system is similar at different epochs but with different rates; in other words, the dynamics of the system could be changing (Marwan *et al.* 2007) (e.g. a non-stationary system with time-varying frequency). As the velocity is further increased to $U^* = 14.0$ in figure 15(*d*), it becomes difficult to identify any well-defined checkerboard or recurrent structures in the RP. Some horizontal curvy lines and their mirrored counterparts become flatter compared to the cases of $U^* = 9.5$ and 10.5,

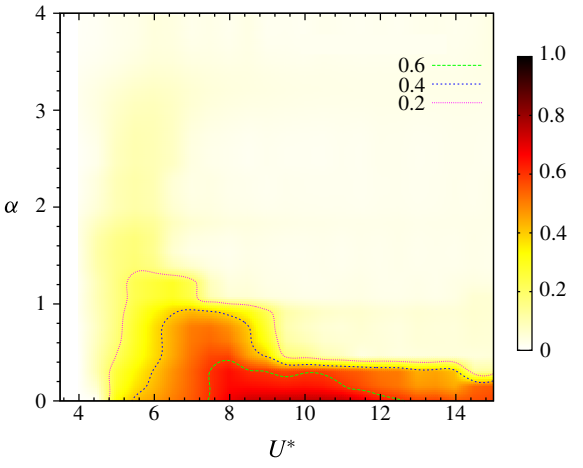

FIGURE 16. (Colour online) The VIV response contour map for a rotating sphere in U^*–α parameter space. Different contour lines depict different amplitude levels as shown in the figure legend.

indicating that some states do not change or change slowly for some time (e.g. for $12 < \tau < 17$). Additionally, the RP exhibits some single points, indicating that the process may be an uncorrelated random or even anti-correlated (Marwan *et al.* 2007). At this point, it can be concluded that the state of the dynamical system becomes chaotic.

As an alternative depiction of the amplitude responses displayed in figure 7, figure 16 shows a response contour map of the sphere vibration in U^*–α parameter space. This clearly shows the shift in high-amplitude response to lower U^* values as the rotation rate is increased. Even though rotation suppresses large-amplitude oscillation as α is increased towards unity, there remains a band of moderate oscillation centred at $U^* \sim 5.5$ that decreases in amplitude much more slowly beyond this α value. Perhaps also of interest is that high-amplitude oscillation is mainly limited to $\alpha \lesssim 0.8$. Previous studies (e.g. Giacobello, Ooi & Balachandar 2009; Kim 2009; Poon *et al.* 2014, and references therein) have shown that the onset of the shear-layer instability wake state of a non-oscillating rotating sphere occurs beyond this α value. That wake state forms when fluid that passes the retreating side of the sphere is pushed towards the other side of the wake to form a distinctive one-sided separating shear layer, thus changing the characteristic formation and release of vortex loops that defines the non-rotating wake state. The nature of the wake state as a function of rotation rate is examined using flow visualisation and particle image velocimetry in § 5.

4.2. *The effective added-mass coefficient and critical mass ratio*

Previous studies of VIV of a circular cylinder have shown the existence of a critical mass ratio, m^*_{crit}, below which large-amplitude body oscillations will persist up to infinite U^* (Govardhan & Williamson 2002; Jauvtis & Williamson 2004). The critical mass ratio can be deduced, as given by Govardhan & Williamson (2002), by evaluating the effective added-mass coefficient C_{EA} in the synchronisation regime. The effective added mass, $m_{EA} = C_{EA} m_d$, is (the negative of) the component of

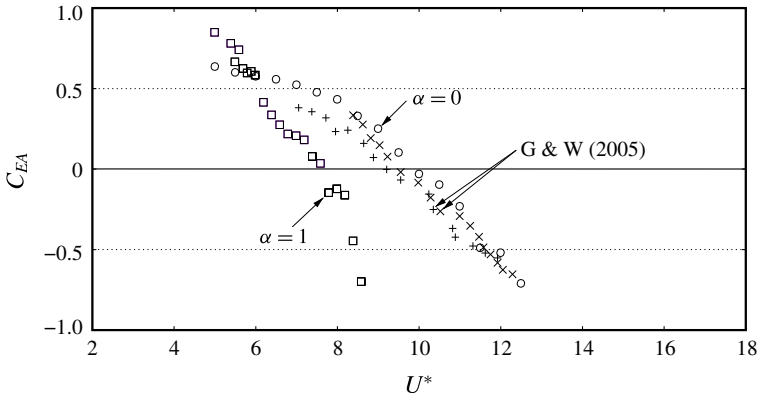

FIGURE 17. Effective added mass as a function of U^* for $\alpha = 0$ (○) and 1 (□). Data from Govardhan & Williamson (2005) for low-mass 2-DOF tethered spheres are provided for comparison (×, $m^* = 1.31$; +, $m^* = 2.83$).

the total force in phase with the acceleration divided by the acceleration. Its significance is that from (3.2) under the condition of low damping, the system frequency depends on the sum of the system mass plus the effective added mass, i.e. $2\pi f = \sqrt{k/(m + m_{EA})}$, hence if $m \to -m_{EA}$, the system response frequency becomes unbounded. Non-dimensionalising this equation and rearranging gives an expression for C_{EA}:

$$C_{EA} = m^* \left(\frac{1 - f^{*2}}{f^{*2}} \right) + \left(\frac{C_A}{f^{*2}} \right), \tag{4.2}$$

in which C_A is the potential-flow added-mass coefficient ($C_A = 0.5$ for a non-rotating or rotating sphere).

For low mass-damping(m^*-ζ) systems, as proposed by Govardhan & Williamson (2002), the critical mass ratio can be evaluated by $m^*_{crit} = \max(-C_{EA})$. Govardhan & Williamson (2002) reported $m^*_{crit} = 0.54$ for 1-DOF transverse VIV of a cylinder and $m^*_{crit} = 0.52$ for the 2-DOF case, and $m^*_{crit} \sim 0.6$ for 2-DOF VIV of a sphere. All these values were reported for very low mass-damping systems ($m^*\zeta \leqslant 0.04$) for moderate Reynolds numbers of $Re \sim 2000$ to $Re \sim 20\,000$. The mass-damping coefficient here is approximately 0.02.

Figure 17 shows the variation of C_{EA} with U^* in the synchronisation range, for the current study with $m^* = 14.2$, for both the non-rotating case ($\alpha = 0$) and a rotating case ($\alpha = 1$). The coefficient C_{EA} is computed using (4.2), in the same manner as in Govardhan & Williamson (2002). Results from the current study are directly compared to previously reported C_{EA} data for sphere vibrations with 2-DOF (tethered spheres) for relatively low mass ratios. It can be observed from the figure that C_{EA} for a non-rotating sphere ($\alpha = 0$) with 1-DOF is similar to that of the 2-DOF case. The mass ratio does not seem to significantly affect C_{EA}, at least for this range of m^*. With imposed rotation, C_{EA} for sphere vibration reduces more quickly with U^*, following the shift in the response curves with rotation rate, as is evident in figure 17. However, the maximum value of $-C_{EA}$ appears similar.

The maximum of $-C_{EA}$ for the cases shown in figure 17 is ∼0.7. Hence, from the above comparison, it can be concluded that the critical mass for both rotating and non-rotating sphere vibration is $m^*_{crit} \sim 0.7$. However, there is some scatter in the

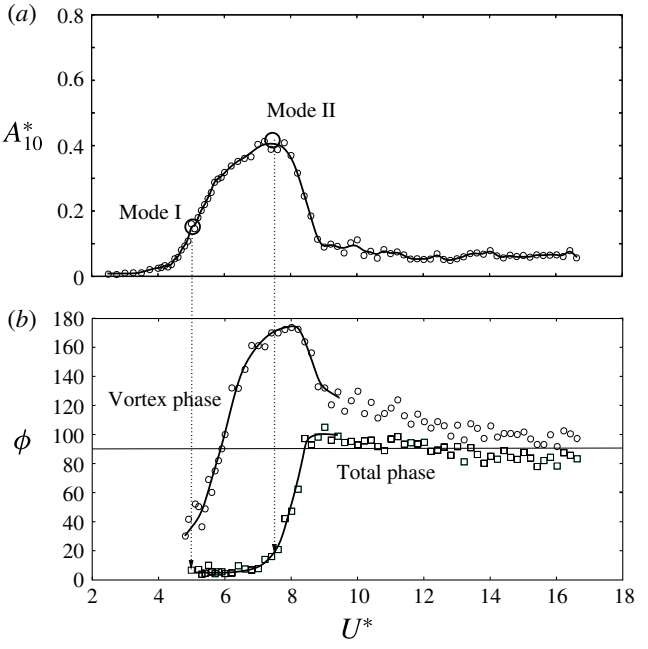

FIGURE 18. Variation of the total phase (ϕ_{total}) and the vortex phase (ϕ_{vortex}) with U^* for $\alpha = 1$. Measured phase variations (*b*), correlated with the amplitude response curve (*a*). The vortex phase starts to rise from low values at the start of Mode I reaching ∼170° near the peak of Mode II. In contrast, the total phase only begins to rise from ∼0° as the response reaches close to the peak values in Mode II. (Compare figure 5).

data, which is consistent with the relatively large mass ratio relative to the critical mass ratio causing the system frequency to depart only slightly from the natural frequency. Thus, the result is not inconsistent with the value of $m^*_{crit} \simeq 0.6$ proposed by Govardhan & Williamson (2002) using much lighter spheres. Perhaps what is more interesting is that the non-rotating and rotating values are similar. The result also seems to suggest that the critical mass is not sensitive to the number of degrees of freedom of oscillation, in agreement with the finding for a circular cylinder.

4.3. *Effect of rotation on the force coefficients*

In this section, the focus is on the effect of transverse rotation on the lift force coefficient for the first two modes within the fundamental synchronisation regime. Results are presented for a selection of rotation rates studied for the same experimental configuration used previously in § 4.1. The dimensionless fluctuating total lift coefficient $C'_{y_{rms}}$, and the total phase (ϕ_{total}) and the vortex phase (ϕ_{vortex}) are defined in accordance with the discussion in § 3.2.

Figure 18 shows the variation of the total phase (ϕ_{total}) and the vortex phase (ϕ_{vortex}) with U^* for $\alpha = 1.0$. It can be observed that the vortex phase (ϕ_{vortex}) starts to rise from low values (∼30–40°) at the start of Mode I reaching ∼170° near the A^*_{10} peak of Mode II. In contrast, the total phase (ϕ_{total}) only starts to rise from ∼0° as the amplitude response reaches close to the peak value in Mode II. These trends were also evident in the non-rotating case shown in figure 5. However, when the vibrations

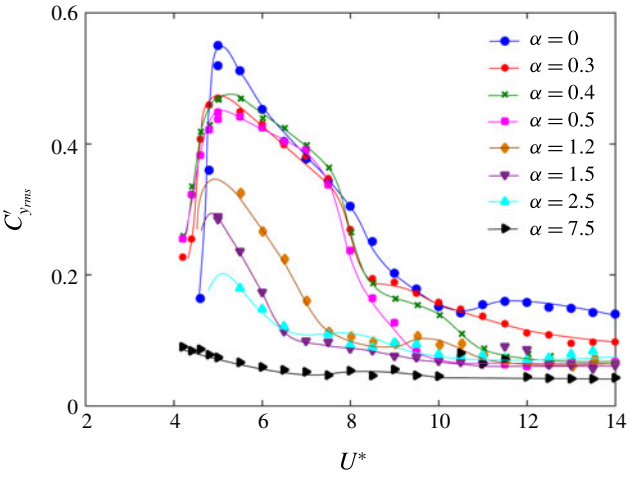

FIGURE 19. (Colour online) Variation of the $C'_{y_{rms}}$ with reduced velocity for different rotation rates.

are suppressed, beyond $U^* = 10$ in this case, both ϕ_{total} and ϕ_{vortex} settle down at approximately 90°. Similar behaviour was observed for other rotation rates as well.

Figure 19 shows the r.m.s. of total lift coefficient $C'_{y_{rms}}$ versus the reduced velocity for various rotation rates. Note that for $\alpha = 7.5$ the signal-to-noise ratio was poor in the force sensor signals due to negligible response of the sphere, hence the theoretical estimate (as discussed in § 2) has been reported for that case. For the non-rotating case ($\alpha = 0$), there is a sudden jump in $C'_{y_{rms}}$ at $U^* \sim 5$ that is associated with the sudden increase in the amplitude response (lock-in), as shown in figure 7. For increasing α, the fluctuating force coefficient decreases monotonically and gradually, in accordance with the decreasing amplitude response, as shown in figure 7. The peak value of $C'_{y_{rms}}$ also decreases gradually with increasing α. For $\alpha = 7.5$, no jump was observed in $C'_{y_{rms}}$, consistent with negligible body oscillations, as shown in figure 7. These observed behaviours of the coefficient $C'_{y_{rms}}$ are consistent with the amplitude response. It appears that the imposed transverse rotation decreases the fluctuating component of the lift force, and in turn, that leads to a decrease in the oscillation amplitude.

Figure 20(*b*) shows the time trace of the total lift force coefficient, C_y, for rotation rate $\alpha = 0.7$, at a reduced velocity of $U^* = 6$, correlated with the sphere displacement (shown in figure 20*a*). As apparent from the figure, there is an evident asymmetry in the force signal as the sphere traverses from the advancing side to the retreating side. This is indicative of the differences in the wake shedding pattern from one half-cycle to the next as the sphere moves from one side to the other. This will be examined further in § 5.

4.3.1. *Competition between the Magnus force and the fluctuating lift force*

The imposed rotation decreases the fluctuating component of the transverse force that drives the oscillations of the sphere. It also increases the mean component of the transverse force due to the Magnus effect. Hence, in order to better understand the dynamics of this problem, the total transverse force coefficient acting on the sphere can be split into two components, as $C_y = \overline{C}_y + C'_{y_{rms}}$, where $\overline{C}_y$ is the time-averaged mean transverse force coefficient and $C'_{y_{rms}}$ is the fluctuating transverse

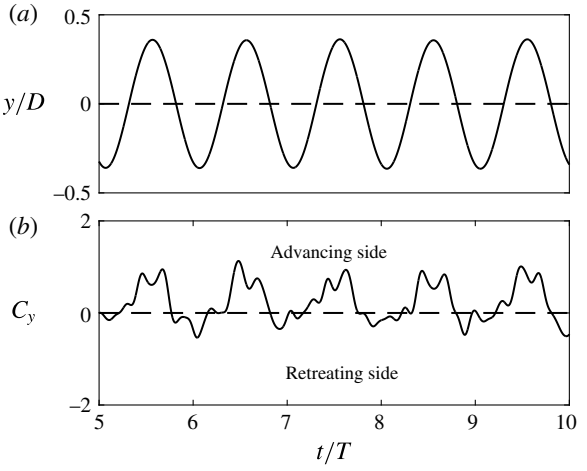

FIGURE 20. Time trace of the total lift coefficient, C_y (b), correlated with the displacement signal (a) for $\alpha = 0.7$ at $U^* = 6$. Asymmetry in the force signal as the sphere traverses from the advancing to the retreating side is evident in the time trace.

force coefficient. Under resonance, where the assumption is often made that (U^*/f^*) and f^* are constant, A^* is directly correlated to C_y for a fixed mass-damping system by

$$A^* \propto \frac{C'_y \sin\phi}{(m_A + C_A)\zeta}, \tag{4.3}$$

where ϕ is the phase difference between the body displacement and transverse force. This can be derived from (2.1), (3.2) and (3.1), as also shown by Williamson & Govardhan (2004). Also, the non-dimensionalised mean displacement of the sphere, $\overline{y}/DU^{*2}$, is directly correlated to the mean transverse force coefficient $\overline{C}_y$ by

$$\frac{\overline{y}}{DU^{*2}} = \frac{\overline{C}_y}{2\pi^3(C_A + m^*)}. \tag{4.4}$$

Initially, for the non-rotating sphere undergoing VIV, $\overline{C}_y$ is zero and $C'_{y_{rms}}$ drives the oscillations. As α is increased, the component of $\overline{C}_y$ increases and the r.m.s. value of the fluctuating component $C'_{y_{rms}}$ decreases. For lower rotation rates, the Magnus effect is not very strong, so there seems to be a competition between the increasing Magnus force and the competing fluctuating transverse force. Such a competition is evident for only lower rotation rates in the current study.

In the left column, figure 21(a–d) shows that the fluctuating oscillation amplitude, A^*, is closely correlated with the fluctuating transverse force coefficient, $C'_{y_{rms}}$, and the non-dimensionalised mean displacement amplitude, $\overline{y}/DU^{*2}$, directly correlates with the mean transverse force coefficient, $\overline{C}_y$, for $\alpha = 0.4$. The right column of figure 21(e–h) shows the same plots for $\alpha = 2.5$. These variations confirm the theoretical relationships given by the two equations above. The response for $\alpha = 0.4$ can be broadly divided into three regimes for this case. In region I, $C'_{y_{rms}}$ is large due to the resonance between the vortex shedding and body oscillation frequencies covering Mode I and the Mode II peak. For this region, $\overline{C}_y$ is reduced

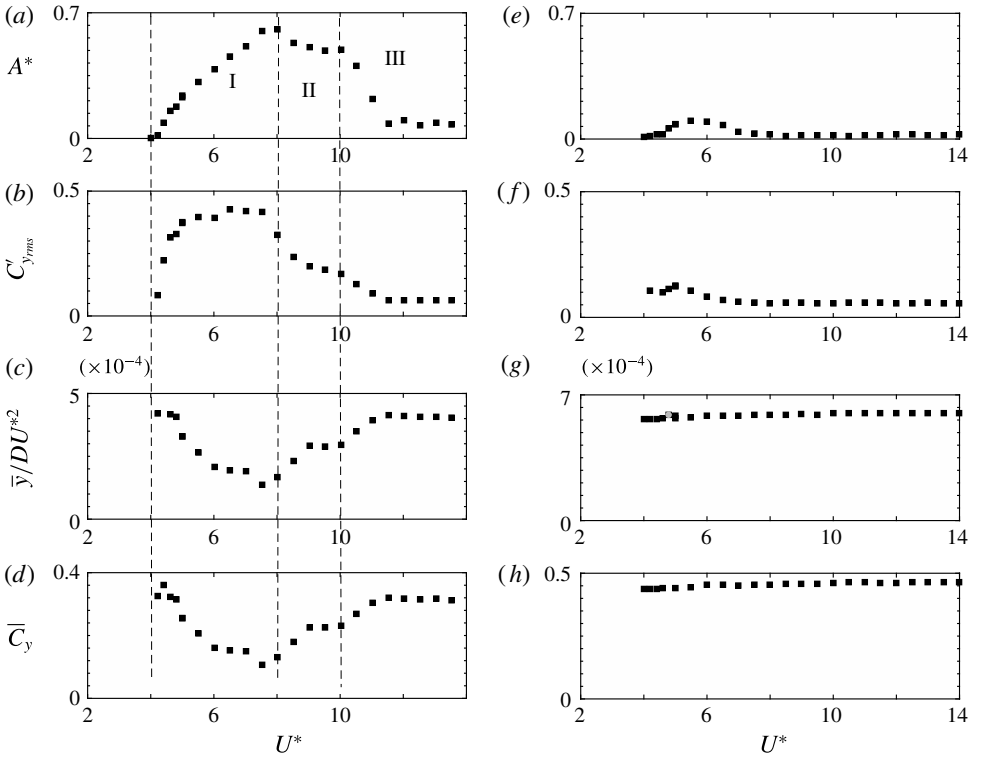

FIGURE 21. Comparison of the response characteristics for $\alpha = 0.4$ (*a–d*) and $\alpha = 2.5$ (*e–h*). The quantity plotted in each row is shown at the left.

with a concomitant effect in $\overline{y}/DU^{*2}$. In region II, which corresponds to the plateau response range after the Mode II peak, the fluctuating forcing is less and the mean force increases, leading to increased mean displacement offset. The competition between the two force components is clearly evident. In region III, the Magnus effect dominates, with $\overline{C}_y$ again reaching a constant value close to that at low U^* before lock-in. Simultaneously, there is sudden drop in the A^* and $C'_{y_{rms}}$ in the desynchronisation regime at high U^*.

The sudden rebound in the amplitude response observed for a rotation rate of $\alpha = 0.3$ at higher U^* values of ∼16–17 (see figure 7) can also be explained on such grounds. A brief study by Sareen *et al.* (2016) investigated the effect of rotation on the force coefficients of a fixed rotating sphere by measuring the drag and lift coefficient for varying rotation rates ($0 \leqslant \alpha \leqslant 6$) at several Reynolds numbers. They observed a sudden drop in the lift coefficient at $\alpha = 0.3$ for a Reynolds number of $Re = 2.75 \times 10^4$. Interestingly, the Reynolds number where the sudden rebound is observed in the current study varies between 2.75×10^4 and 2.9×10^4 corresponding to the U^* range 16–17. Thus, it can be conjectured that here also there is a sudden drop in the mean lift force acting on the sphere at $\alpha = 0.3$ for $U^* \sim 16$–17. In lieu of the competition between the mean lift force and the fluctuating force, the fluctuating force is allowed to suddenly increase leading to a sudden rebound in the amplitude response.

However, at higher rotation rates, for example at $\alpha = 2.5$ as shown in figure 21, the Magnus force dominates over the entireU^* range, even though there is a narrow

resonant regime. This leads to almost constant values of $\bar{y}/DU^{*^2}$ and $\overline{C}_y$. For this case, A^* and $C_{y_{rms}}'$ remain at low values over the entire U^* range. How the sphere rotation affects vortex shedding and thereby leads to the attenuation of VIV will be discussed in § 5.

5. Modes of vortex formation

The wake of a stationary sphere at high Reynolds number ($Re \gtrsim 1000$) is highly unsteady and chaotic. It is characterised by interlinked vortex rings or hairpin loops emanating from the surface of the sphere at an azimuthal location that changes from cycle to cycle. The low Reynolds number precursor structures have been observed previously in the dye visualisations of the wake of a liquid drop of Magarvey & Bishop (1961), and further experiments of Sakamoto & Haniu (1990), Leweke *et al.* (1999) and Ormières & Provansal (1999). Interlinked vortex loops have also been reported in numerical simulations concerning the wake of a static sphere by Tomboulides, Orszag & Karniadakis (1993), Johnson & Patel (1999), Mittal (1999) and Thompson, Leweke & Provansal (2001).

Similar vortex loops have also been observed in the wake of an elastically mounted sphere undergoing VIV. Previous visualisations of a rising bubble by Brücker (1999) suggested that the wake consisted of hairpin vortices. Sakamoto & Haniu (1990) also observed a similar two-sided chain of vortex loops with alternating signs. Vorticity measurements by Govardhan & Williamson (2005) showed planar symmetric vortex loops (hairpins) of opposite sign emanating from the two sides of a non-rotating sphere undergoing VIV. The central distinction between the wake behind a static sphere and an oscillating sphere is that in the case of an oscillating sphere, the loops have a preferred orientation and maintain a symmetry with the horizontal plane containing the principal transverse vibration. Lee *et al.* (2013) covered a wide range of Reynolds number $50 \leqslant Re \leqslant 12\,000$ and classified the flow and response of a neutrally buoyant tethered sphere in various regimes depending on the Reynolds number. They also observed unsteady helix-shaped vortical structures in the wake at higher Reynolds number, presumably associated with the neutral buoyancy of the sphere.

But what happens if we impose a transverse rotation to the sphere while it undergoes VIV? From previous studies on rigidly mounted spheres, it is known that the transverse rotation imposes strong asymmetry in the wake, causing the loops to bend towards the advancing side (the side of the sphere moving in the direction opposite to the fluid) of the sphere due to the Magnus effect (Magnus 1853), which in consequence increases the 'lift force' towards the retreating side (the side of the sphere moving in the same direction as the fluid). Previous numerical studies by Giacobello *et al.* (2009), Kim (2009) and Poon *et al.* (2014) reported suppression of the vortex shedding for a certain range of rotation rates that depended on the Reynolds number. However, when α was increased, the vortex shedding resumed, although it was very different to the vortex shedding at lower α values that is associated with the 'buildup and release' of the recirculation bubbles behind the sphere. From examining the velocity and vorticity fields near the surface, they conjectured the shedding to be a shear-layer instability of the Kelvin–Helmholtz type. The flow at such high α values is characterised by single-sided shedding at the advancing side of the sphere.

There have been only a few experimental studies on rigidly mounted rotating spheres at very high Reynolds numbers ($Re \geqslant 6 \times 10^4$) (e.g. Macoll 1928; Barlow & Domanski 2008; Kim *et al.* 2014; Kray, Franke & Frank 2014). All these studies

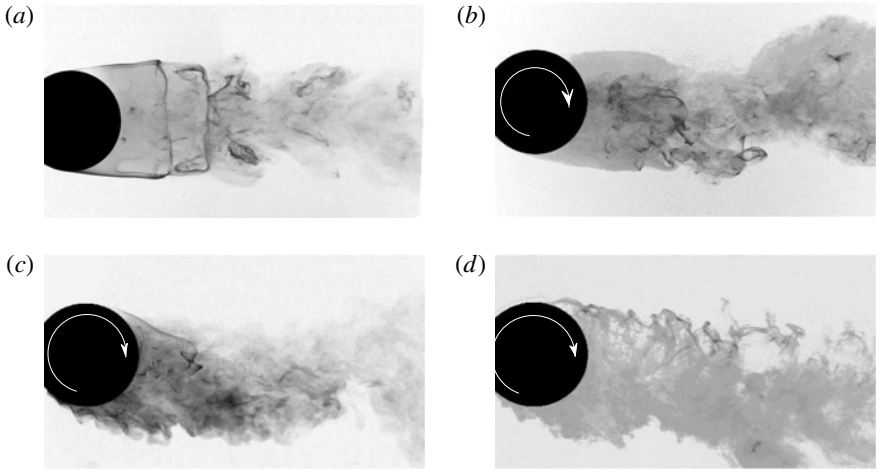

FIGURE 22. Dye visualisation images of a rigidly mounted (non-VIV case) rotating sphere at $Re = 3510$ for (*a*) $\alpha = 0$, (*b*) $\alpha = 0.2$, (*c*) $\alpha = 1.5$ and (*d*) $\alpha = 3$. Flow is from left to right. The deflection of the wake in the direction of rotation is evident from the images. For $\alpha = 3$, the near wake becomes wider than the smaller α cases.

focused on the effect of the rotation rate on the force coefficients for understanding the inverse Magnus effect observed at such high Reynolds numbers. They found that the rotation causes asymmetry between the boundary layer separation at the retreating side and the advancing side of the sphere. There was no consensus as to whether the rotation suppresses the vortex shedding at such high Reynolds numbers or not. Figure 22 shows the effect of rotation on a rigidly mounted sphere for a Reynolds number of $Re = 3510$, using dye visualisation. The vectoring of the wake towards the advancing side is clearly evident. Between $\alpha = 1.5$ and 3, the deflection does not increase further, although the near wake increases in width with the retreating side separating shear layer becoming less well defined.

The question arises, how does the transverse rotation change the wake patterns behind an elastically mounted sphere undergoing VIV? What causes the VIV response to be suppressed? In order to get an insight into the underlying flow dynamics, hydrogen-bubble visualisations were undertaken in the equatorial plane of the sphere to gauge the effect of rotation.

Figure 23 shows instantaneous hydrogen-bubble flow visualisation images for the elastically mounted rotating sphere in the equatorial plane for $U^* = 6$ (Mode I) at $\alpha = 0$, 1, 2.5 and 6. The flow is from left to right and the sphere is rotating anti-clockwise. The first column shows images for the instant when the sphere is at the peak of one cycle (phase of π) in the y direction and the second column shows the images for the instant when the sphere reaches the peak amplitude in the opposite direction (phase of $3\pi/2$). The centreline has been overlaid in the images to show the wake deflection more clearly. Some visually identified structures have been marked in red. Since the flow at high Reynolds numbers is three-dimensional and chaotic, the hydrogen bubbles do not necessarily stay in the laser plane. In spite of this, some structures are identifiable and the broad flow dynamics can be readily interpreted from these visualisations.

For $\alpha = 0$, in case (*a*), the wake is deflected upwards when the sphere reaches the peak displacement, and as the phase changes from π to $3\pi/2$, the wake changes

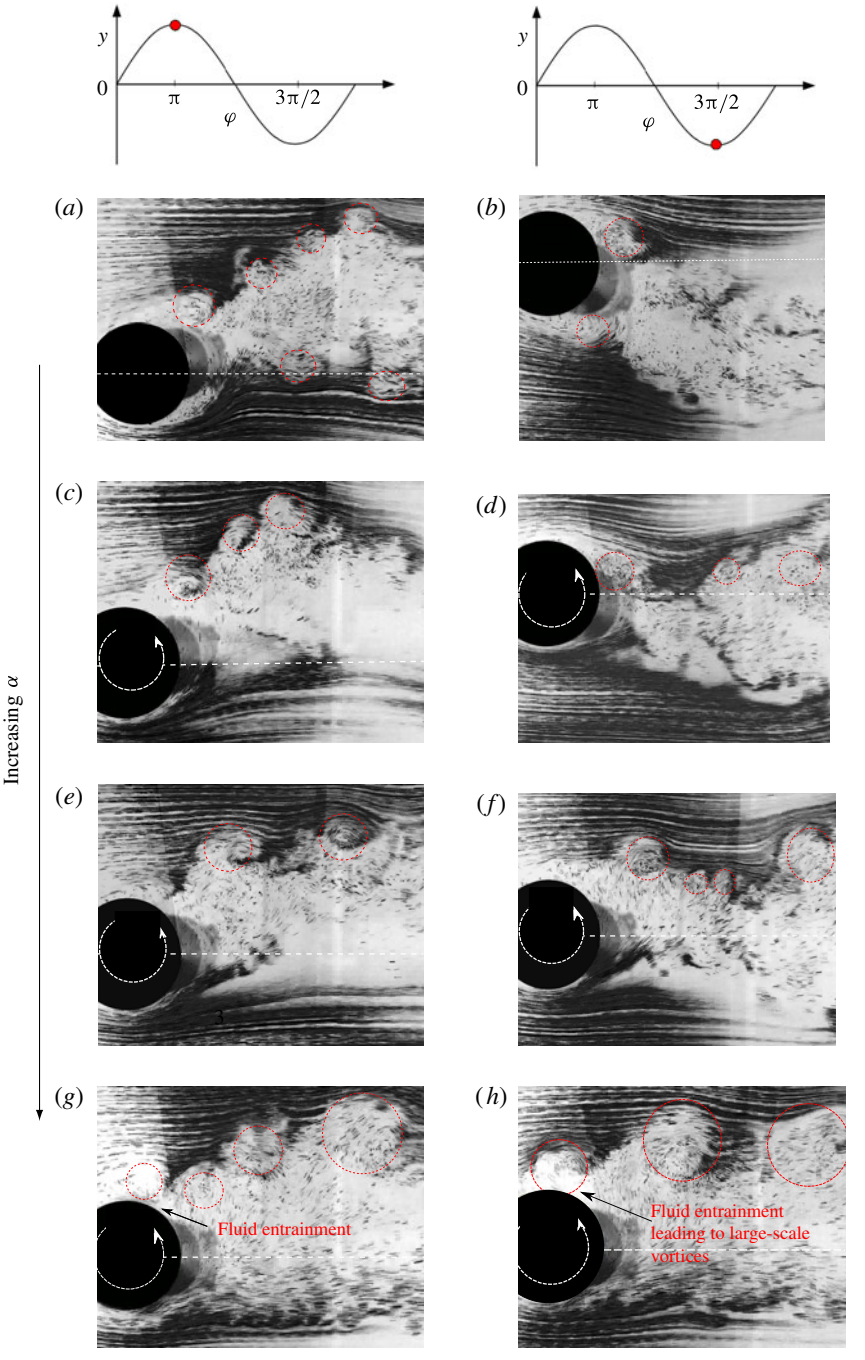

FIGURE 23. (Colour online) Instantaneous images of the hydrogen-bubble visualisation in the equatorial plane for the following cases: (a,b) $U^* = 6$, $\alpha = 0$, (c,d) $U^* = 6$, $\alpha = 1$, (e,f) $U^* = 6$, $\alpha = 2.5$, (g,h) $U^* = 6$, $\alpha = 6$. Panels (a,c,e,g) show images when the sphere is at its lowest position, and (b,d,f,h) when it is at its highest position.

orientation from upwards to downwards. The wake deflection is symmetrical, as expected for a non-rotating oscillating sphere undergoing VIV. The wake deflection and sphere displacement are in the opposite direction. Also, the roll-up of the separating shear layers just behind the sphere on both the sides can be seen, which convect downstream as vortical structures (shown in the horizontal cut through the interlinked vortex loops present in the wake).

As α is increased from 0 to 6, the wake structure changes. As shown in figure 23(*a*,*c*,*e*,*g*), the deflection increases (towards the advancing side) and the wake widens due to the rotation of the sphere in the anti-clockwise direction (Magnus effect). Due to this rotation-induced forcing, the mean displacement of the sphere shifts towards the retreating side of the sphere (see § 4.1).

With increased rotation, the flow from the retreating side is vectored towards the advancing side. The flow is continuously drawn upwards by the sphere rotation; the flow structures, therefore, exhibit a large-scale shedding pattern. Case (*g*) clearly shows very large-scale vortices shed at the advancing side of the sphere for $\alpha = 6$, when the VIV is greatly suppressed.

With increased entrainment of fluid from the retreating side to the advancing side, it can be conjectured that the shear layer becomes unstable, and the vortices are shed further upstream with increasing rotation, as is evident in case (*g*). At high rotation rates, e.g. case (*e*) and case (*f*), the recirculation bubble is evidently mostly suppressed. This near wake is very similar to the 'shear-layer instability' regime reported by Giacobello *et al.* (2009), Kim (2009) and Poon *et al.* (2014) for rigidly mounted rotating spheres at low Reynolds number ($Re \leqslant 1000$). They reported single-sided shedding on the advancing side of the rotating sphere. They also observed suppression of the recirculation bubbles and the large-scale shedding patterns with increasing rotation.

For the phase of $3\pi/2$ (cases *b*,*d*,*f*,*h*), as α increases from 0 (case *b*) to 1 (case *d*), the downward deflection of the wake decreases. For $\alpha = 2.5$, the wake is rather deflected slightly upwards and for $\alpha = 6$, the wake is highly deflected towards the advancing side. Since the wake is always deflected towards the advancing side for all shedding cycles, there is little oscillating force acting on the sphere to induce sizeable vibrations. This is also evident in measurements of the r.m.s. of the transverse fluctuating force coefficient $C'_{y_{rms}}$ reported in § 4.3. Figure 19 shows $C'_{y_{rms}}$ is negligible for $U^* = 6$ at $\alpha = 6$. Hence, VIV is (almost) suppressed for $\alpha = 6$ (case *h*) and the sphere is displaced towards the retreating side.

Owing to the fact that hydrogen-bubble visualisations provide mostly qualitative information, particle image velocimetry (PIV) was employed in the central equatorial plane (plane of symmetry) to provide more quantitative information, allowing an alternative view of the main near-wake features. Figure 24 shows representative near-wake vorticity maps, phase-averaged over more than 100 oscillation cycles, in the central equatorial plane for the same experimental conditions as shown in figure 23. As is evident from figure 24(*a*,*b*), the phase-averaged wake of a non-rotating oscillating sphere consists of a counter-rotating vortex pair downstream that represents a cut through a vortex ring, as previously reported by Govardhan & Williamson (2005). The deflections observed in the overall wake patterns in all cases are consistent with those observed earlier using the hydrogen-bubble visualisations (figure 23). For $\alpha = 0$, the wake deflections at opposite ends of the oscillation cycle are symmetric, but they becomes increasingly unsymmetric with increasing α, until for $\alpha = 6$ the vibrations are almost suppressed. The wake at $\alpha = 6$ is considerably wider than the other cases. For the phase of $3\pi/2$, as the rotation rate increases from $\alpha = 0$ to 1, it can clearly be

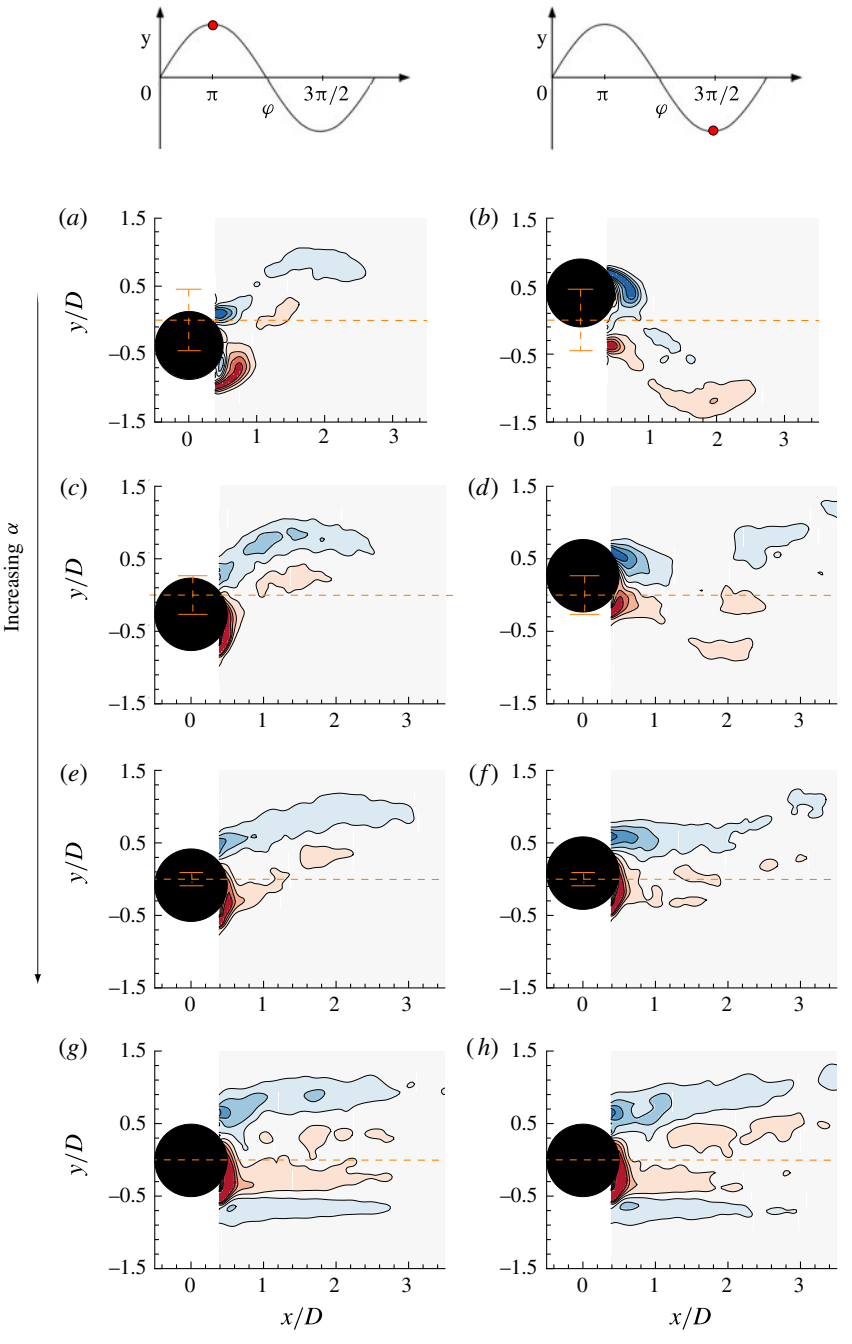

FIGURE 24. (Colour online) Equatorial near-wake vorticity maps obtained from phase-averaged PIV for the following cases: (*a*,*b*) $U^* = 6$, $\alpha = 0$, (*c*,*d*) $U^* = 6$, $\alpha = 1$, (*e*,*f*) $U^* = 6$, $\alpha = 2.5$ and (*g*,*h*) $U^* = 6$, $\alpha = 6$. Panels (*a*,*c*,*e*,*g*) show images corresponding to when the sphere is at its lowest position, and (*b*,*d*,*f*,*h*) when it is at its highest position. The blue contours show clockwise vorticity and red contours show anti-clockwise vorticity. The normalised vorticity range is $\omega^* = \omega D/U$ (where ω is the vorticity) $\in [-3, 3]$ for $\alpha = 0$, $[-2, 2]$ for $\alpha = 1$ and $\alpha = 2.5$ and $[-1, 1]$ for $\alpha = 6$.

seen that the wake deflection angle towards the retreating side (downwards) decreases. When α is further increased to 2.5, the downward deflection angle is almost zero. For $\alpha = 6$, the wake is now deflected in the opposite direction (advancing side). The presence of anti-clockwise vorticity encircling the sphere on the retreating side points towards highly vectored flow from the retreating to the advancing side. Also, the recirculation region is absent for higher rotation rates. These findings are congruous with the more qualitative hydrogen-bubble visualisations.

Although the wake of a sphere is intrinsically highly three-dimensional and chaotic at such high Reynolds numbers, the flow visualisations in the plane of symmetry (equatorial plane) still provide important insights into the underlying flow dynamics.

6. Conclusions

An extensive series of experiments and flow visualisations have been performed to study the effect of transverse rotation on the VIV response of a sphere. Transverse rotation was imposed such that the axis of rotation was perpendicular to the flow direction. The vibration response was studied for a wide parameter space of $0 \leqslant \alpha \leqslant 7.5$ and $3 \leqslant U^* \leqslant 18$. Interestingly, unlike its two-dimensional counterpart, the cylinder, the VIV response of the sphere reduced gradually and steadily with increasing the rotation ratio, leading to an almost complete suppression for $\alpha \geqslant 6.0$. With some similarities to the non-rotating case, the amplitude response of a rotating sphere exhibited a bell-shaped curve, showing vibration Modes I and II for $\alpha \leqslant 1$. It was also found that the synchronisation regime became narrower with increasing α, and also the peak amplitude response gradually decreased almost linearly for $\alpha \lesssim 1$. For $\alpha \geqslant 0.5$, the amplitude response dropped off rapidly with increasing U^* as soon as the peak response was reached, whereas, for lower rotation ratios of $\alpha \leqslant 0.4$, large oscillation amplitudes were still encountered at higher U^* values after the A^* peak was reached in Mode II. The oscillation frequency remained close to the natural frequency of the system for all cases.

Furthermore, it was found that oscillation amplitudes not only decreased but also the oscillations became less periodic with increasing rotation. Recurrence analysis revealed a transition from periodic to chaotic in the recurrence map complementing the occurrence of broadband frequency spectra at the onset of bifurcation. The time-averaged mean displacement increased towards the retreating side of the sphere with increasing α, due to an increase in the mean Magnus force. A substantial jump in fluctuating lift force coefficient, $C_{y_{rms}}'$, was observed when lock-in occurred at the start of the Mode I response. The peak value of $C_{y_{rms}}'$ as U^* was increased was found to decrease consistently with the rotation rate, following a trend similar to that of the vibration amplitude. Imposed rotation increased the mean component of the transverse force ($\overline{C}_y$) due to the Magnus effect. It simultaneously decreased the fluctuating component of the transverse force ($C_{y_{rms}}'$), which decreased the VIV response.

Compared to VIV of a low mass-damped cylinder, the total and vortex phase transitions are much less sharp, as the VIV mode changes. However, overall the phase transitions are similar. The vortex phase jumps as the response changes from Mode I to Mode II, and the total phase jumps from low to high values as the Mode II vibration transitions to the lower plateau, which is only observed for $\alpha \lesssim 0.4$.

Flow visualisations using hydrogen bubbles and the PIV techniques were performed in the equatorial plane containing the principal transverse vibration. With increased rotation, the wake deflected more and more towards the advancing side of the sphere.

The flow was continuously drawn from the retreating side to the advancing side of the sphere with increasing rotation rate, which led to entrainment of fluid at the advancing side. This entrainment gave rise to large-scale one-sided vortex shedding. This flow behaviour is very similar to the 'shear-layer instability' regime reported by previous studies for rigidly mounted rotating spheres. For the rotation rates where the VIV was found to be completely suppressed, the wake was found to be always deflected towards the advancing side with large-scale flow structures for all shedding cycles. A lack of an oscillating force acting on the sphere led to near suppression of the VIV. This also led to a shift in the mean displacement of the sphere towards the retreating side. Measurements of the fluctuating transverse force coefficients $C'_{y_{rms}}$ and $\overline{C}_y$ were also consistent with the flow visualisation observations.

Acknowledgements

The authors would like to acknowledge the financial support from the Australian Research Council Discovery Project grants (DP150102879 and DP170100275). A.S. acknowledges the support of a Monash Graduate Scholarship (MGS) and a Monash International Postgraduate Research Scholarship (MIPRS).

REFERENCES

BARLOW, J. B. & DOMANSKI, M. J. 2008 Lift on stationary and rotating spheres under varying flow and surface conditions. *AIAA J.* **46** (8), 1932–1936.

BEARMAN, P. W. 1984 Vortex shedding from oscillating bluff bodies. *Annu. Rev. Fluid Mech.* **16** (1), 195–222.

BEHARA, S., BORAZJANI, I. & SOTIROPOULOS, F. 2011 Vortex-induced vibrations of an elastically mounted sphere with three degrees of freedom at $Re = 300$: hysteresis and vortex shedding modes. *J. Fluid Mech.* **686**, 426–450.

BEHARA, S. & SOTIROPOULOS, F. 2016 Vortex-induced vibrations of an elastically mounted sphere: the effects of Reynolds number and reduced velocity. *J. Fluids Struct.* **66**, 54–68.

BLEVINS, R. D. 1990 *Flow-Induced Vibration*, 2nd edn. Krieger Publishing Company.

BOURGUET, R. & LO JACONO, D. 2014 Flow-induced vibrations of a rotating cylinder. *J. Fluid Mech.* **740**, 342–380.

BRÜCKER, C. 1999 Structure and dynamics of the wake of bubbles and its relevance for bubble interaction. *Phys. Fluids* **11** (7), 1781–1796.

ECKMANN, J., KAMPHORST, S. O. & RUELLE, D. 1987 Recurrence plots of dynamical systems. *Europhys. Lett.* **4** (9), 973–977.

FOURAS, A., LO JACONO, D. & HOURIGAN, K. 2008 Target-free stereo PIV: a novel technique with inherent error estimation and improved accuracy. *Exp. Fluids* **44** (2), 317–329.

GIACOBELLO, M., OOI, A. & BALACHANDAR, S. 2009 Wake structure of a transversely rotating sphere at moderate Reynolds numbers. *J. Fluid Mech.* **621**, 103–130.

GOVARDHAN, R. & WILLIAMSON, C. H. K. 1997 Vortex-induced motions of a tethered sphere. *J. Wind Engng Indust. Aerodyn.* **375**, 69–71.

GOVARDHAN, R. & WILLIAMSON, C. H. K. 2000 Modes of vortex formation and frequency response of a freely vibrating cylinder. *J. Fluid Mech.* **420**, 85–130.

GOVARDHAN, R. & WILLIAMSON, C. H. K. 2002 Resonance forever: existence of a critical mass and an infinite regime of resonance in vortex-induced vibration. *J. Fluid Mech.* **473**, 147–166.

GOVARDHAN, R. N. & WILLIAMSON, C. H. K. 2005 Vortex-induced vibrations of a sphere. *J. Fluid Mech.* **531**, 11–47.

VAN HOUT, R., KATZ, A. & GREENBLATT, D. 2013*a* Acoustic control of vortex-induced vibrations of a tethered sphere. *Phys. Fluids* **25**, 077102.

VAN HOUT, R., KATZ, A. & GREENBLATT, D. 2013*b* Time-resolved particle image velocimetry measurements of vortex and shear layer dynamics in the near wake of a tethered sphere. *Phys. Fluids* **25** (7), 077102.

VAN HOUT, R., KRAKOVICH, A. & GOTTLIEB, O. 2010 Time resolved measurements of vortex-induced vibrations of a tethered sphere in uniform flow. *Phys. Fluids* **22** (8), 087101.

HOVER, F. S., MILLER, S. N. & TRIANTAFYLLOU, M. S. 1997 Vortex-induced vibration of marine cables: experiments using force feedback. *J. Fluids Struct.* **11** (3), 307–326.

JAUVTIS, N., GOVARDHAN, R. & WILLIAMSON, C. H. K. 2001 Multiple modes of vortex-induced vibration of a sphere. *J. Fluids Struct.* **15** (3–4), 555–563.

JAUVTIS, N. & WILLIAMSON, C. H. K. 2004 The effect of two degrees of freedom on vortex-induced vibration at low mass and damping. *J. Fluid Mech.* **509**, 23–62.

JOHNSON, T. A. & PATEL, V. C. 1999 Flow past a sphere up to a Reynolds number of 300. *J. Fluid Mech.* **378**, 19–70.

KHALAK, A. & WILLIAMSON, C. H. K. 1999 Motions, forces and mode transitions in vortex-induced vibrations at low mass-damping. *J. Fluids Struct.* **13** (7–8), 813–851.

KIM, D. 2009 Laminar flow past a sphere rotating in the transverse direction. *J. Mech. Sci. Technol.* **23** (2), 578–589.

KIM, J., CHOI, H., PARK, H. & YOO, J. Y. 2014 Inverse Magnus effect on a rotating sphere: when and why. *J. Fluid Mech.* **754**, R2.

KRAKOVICH, A., ESHBAL, L. & VAN HOUT, R. 2013 Vortex dynamics and associated fluid forcing in the near wake of a light and heavy tethered sphere in uniform flow. *Exp. Fluids* **54** (11), 1615.

KRAY, T., FRANKE, J. & FRANK, W. 2012 Magnus effect on a rotating sphere at high Reynolds numbers. *J. Wind Engng Indust. Aerodyn.* **110**, 1–9.

KRAY, T., FRANKE, J. & FRANK, W. 2014 Magnus effect on a rotating soccer ball at high Reynolds numbers. *J. Wind Engng Indust. Aerodyn.* **124**, 46–53.

LEE, H., HOURIGAN, K. & THOMPSON, M. C. 2013 Vortex-induced vibration of a neutrally buoyant tethered sphere. *J. Fluid Mech.* **719**, 97–128.

LEWEKE, T., PROVANSAL, M., ORMIERES, D. & LEBESCOND, R. 1999 Vortex dynamics in the wake of a sphere. *Phys. Fluids* **11** (9), S12.

LIGHTHILL, J. 1986 Fundamentals concerning wave loading on offshore structures. *J. Fluid Mech.* **173**, 667–681.

MACOLL, J. W. 1928 Aerodynamics of a spinning sphere. *J. R. Aero. Soc.* **28**, 777–798.

MAGARVEY, R. H. & BISHOP, R. L. 1961 Transition ranges for three-dimensional wakes. *Can. J. Phys.* **39** (10), 1418–1422.

MAGNUS, G. 1853 Ueber die Abweichung der Geschosse, und: Ueber eine auffallende Erscheinung bei rotirenden Körpern. *Annalen der Physik* **164** (1), 1–29.

MARWAN, N. 2003 Encounters with neighbours: current developments of concepts based on recurrence plots and their applications. PhD thesis, Universität Potsdam.

MARWAN, N. 2008 A historical review of recurrence plots. *Eur. Phys. J.* **164** (1), 3–12.

MARWAN, N., ROMANO, M., THIEL, M. & KURTHS, J. 2007 Recurrence plots for the analysis of complex systems. *Phys. Rep.* **438** (5), 237–329.

MIRAUDA, D., VOLPE PLANTAMURA, A. & MALAVASI, S. 2014 Dynamic response of a sphere immersed in a shallow water flow. *J. Offshore Mech. Arctic Engng* **136** (2), 021101.

MITTAL, R. 1999 A Fourier–Chebyshev spectral collocation method for simulating flow past spheres and spheroids. *Intl J. Numer. Meth. Fluids* **30** (7), 921–937.

MORSE, T., GOVARDHAN, R. & WILLIAMSON, C. H. K. 2008 The effect of end conditions on the vortex-induced vibration of cylinders. *J. Fluids Struct.* **24** (8), 1227–1239.

NAUDASCHER, E. & ROCKWELL, D. 2012 *Flow-Induced Vibrations: An Engineering Guide*. Courier Corporation.

ORMIÈRES, D. & PROVANSAL, M. 1999 Transition to turbulence in the wake of a sphere. *Phys. Rev. Lett.* **83** (1), 80.

PAÏDOUSSIS, M. P., PRICE, S. & DE LANGRE, E. 2010 *Fluid–Structure Interactions: Cross-Flow-Induced Instabilities*. Cambridge University Press.

POON, E. K. W., OOI, A. S., GIACOBELLO, M., IACCARINO, G. & CHUNG, D. 2014 Flow past a transversely rotating sphere at Reynolds numbers above the laminar regime. *J. Fluid Mech.* **759**, 751–781.

PREGNALATO, C. J. 2003 Flow-induced vibrations of a tethered sphere. PhD thesis, Monash University.

RAO, A., PASSAGGIA, P.-Y., BOLNOT, H., THOMPSON, M., LEWEKE, T. & HOURIGAN, K. 2012 Transition to chaos in the wake of a rolling sphere. *J. Fluid Mech.* **695**, 135–148.

SAKAMOTO, H. & HANIU, H. 1990 A study on vortex shedding from spheres in a uniform flow. *J. Fluids Engng* **112** (4), 386–392.

SAREEN, A., ZHAO, J., LO JACONO, D., SHERIDAN, J., HOURIGAN, K. & THOMPSON, M. C. 2016 Flow past a transversely rotating sphere. In *Proceedings of the 11th International Conference on Flow-Induced Vibration and Noise, The Hague, The Netherlands, 4–6 July 2016*. The Netherlands Organisation for Applied Scientific Research.

SARPKAYA, T. 2004 A critical review of the intrinsic nature of vortex-induced vibrations. *J. Fluids Struct.* **19** (4), 389–447.

SEYED-AGHAZADEH, B. & MODARRES-SADEGHI, Y. 2015 An experimental investigation of vortex-induced vibration of a rotating circular cylinder in the crossflow direction. *Phys. Fluids* **27** (6), 067101.

THOMPSON, M. C., LEWEKE, T. & PROVANSAL, M. 2001 Kinematics and dynamics of sphere wake transition. *J. Fluids Struct.* **15** (3), 575–585.

TOMBOULIDES, A., ORSZAG, S. & KARNIADAKIS, G. 1993 Direct and large-eddy simulations of axisymmetric wakes. In *31st Aerospace Sciences Meeting*, p. 546. AIAA.

WILLIAMSON, C. H. K. & GOVARDHAN, R. 1997 Dynamics and forcing of a tethered sphere in a fluid flow. *J. Fluids Struct.* **11**, 293–305.

WILLIAMSON, C. H. K. & GOVARDHAN, R. 2004 Vortex-induced vibrations. *Annu. Rev. Fluid Mech.* **36** (1), 413–455.

WONG, K. W. L., ZHAO, J., LO JACONO, D., THOMPSON, M. C. & SHERIDAN, J. 2017 Experimental investigation of flow-induced vibration of a rotating circular cylinder. *J. Fluid Mech.* **829**, 486–511.

ZHAO, J., LEONTINI, J. S., LO JACONO, D. & SHERIDAN, J. 2014*a* Chaotic vortex induced vibrations. *Phys. Fluids* **26** (12), 121702.

ZHAO, J., LEONTINI, J. S., LO JACONO, D. & SHERIDAN, J. 2014*b* Fluid–structure interaction of a square cylinder at different angles of attack. *J. Fluid Mech.* **747**, 688–721.